A catastrophic flowslide overridden on liquefied substrate: The 1983 Saleshan landslide, China

Fanyu Zhang[1,1], Jianbing Peng[2,2], Xiugang Wu[1,1], Fazhen Pan[1,1], Yao Jiang[3,3], Chao Kang[4,4], Weijiang Wu[5,5], and Wenguo Ma[6,6]

[1]Lanzhou University
[2]Chang'an University
[3]Institute of Mountain Hazards and Environment, Chinese Academy of Sciences
[4]University of Alberta
[5]Geological Hazards Research and Prevention Institute, Gansu Academy of Sciences
[6]School of Physics and Electronic-Electrical Engineering, Ningxia University

November 30, 2022

Abstract

A flowslide overriding liquefied substrate can vastly enhance its disaster after failure initiation, due to rapid velocity and long-runout distance during landslides mobilized into flows. It is crucial to provide improved understanding to the mechanism of these catastrophic flowslides for hazard mitigation and risk assessment. This study focuses on the Saleshan landslide of Gansu in China, which is a typically catastrophic flowslide overrode a liquefied sand substrate. Geomorphologic and topographic maps along with analysis of seismic signals confirm its dynamic features and mobilized behaviors. ERT surveying detected abundant groundwater in the landslide, which is fundamental to its rapid long-runout distance. Particle size distributions and triaxial shear behaviors affirmed more readily liquefied behavior of superficial loess and underlying alluvial sand than red soil sandwiched them. We also examined the liquefaction susceptibility of the alluvial sand under loading impact at undrained and drained conditions. The alluvial sand is readily liquefied in the undrained condition while it is difficult at drained condition due to rapid water pore pressure dissipation. The results showed that the landslide experienced a sudden transformation from slide on the steep slope where it originated to flow on a nearly flat terrace with abundant groundwater that it overrode. This transformation can be attributed to the liquefied alluvial sand substrate enhancing the whole landslide body mobility. Along with recent, similar findings from landslides worldwide, substrate liquefaction may present a widespread, significant increase in landslide hazard and consequent mobility and our study reveals conditions necessary for this phenomenon to occur.

Title: A catastrophic flowslide overridden on liquefied substrate: The 1983 Saleshan landslide in China

Authors: Fanyu Zhang, Jianbing Peng, Xiugang Wu, Fazhen Pan, Yao Jiang, Chao Kang, Weijiang Wu, Wenguo Ma

Abstract: A flowslide overriding liquefied substrate can vastly enhance its disaster after failure initiation, due to rapid velocity and long-runout distance during landslides mobilized into flows. It is crucial to provide improved understanding to the mechanism of these catastrophic flowslides for hazard mitigation and risk assessment. This study focuses on the Saleshan landslide of Gansu in China, which is a typically catastrophic flowslide overrode a liquefied sand substrate. Geomorphologic and topographic maps along with analysis of seismic signals confirm its dynamic features and mobilized behaviors. ERT surveying detected abundant groundwater in the landslide, which is fundamental to its rapid long-runout distance. Particle size distributions and triaxial shear behaviors affirmed more readily liquefied behavior of superficial loess and underlying alluvial sand than red soil sandwiched them. We also examined the liquefaction susceptibility of the alluvial sand under loading impact at undrained and drained conditions. The alluvial sand is readily liquefied in the undrained condition while it is difficult at drained condition due to rapid water pore pressure dissipation. The results showed that the landslide experienced a sudden transformation from slide on the steep slope where it originated to flow on a nearly flat terrace with abundant groundwater that it overrode. This transformation can be attributed to the liquefied alluvial sand substrate enhancing the whole landslide body mobility. Along with recent, similar findings from landslides worldwide, substrate liquefaction may present a widespread, significant increase in landslide hazard and consequent mobility and our study reveals conditions necessary for this phenomenon to occur.

Keywords: Catastrophic flowslide, liquified substrate, mobilized transformation, Saleshan landslide, China

1. Introduction

Flowslide is generally catastrophic worldwide. This kind of flow-like landslides is always characterized by rapid velocity and long-runout distance during landslides mobilized into flows, as such they usually cause more catastrophic threats to people, environment, and property. Hence, it is curial to understand the mobility of these catastrophic flowslides to hazard mitigation and risk assessment.

Some studies have been conducted to gain understanding of rapid long-runout flowslides, involving field evidences, numerical and physical simulations, and shear tests, along with very few field monitoring (Hutchinson and Bhandari, 1971; Misfeldt *et al.*, 1991; Evans *et al.*, 2001; Wang *et al.*, 2003; Hungr and Evans, 2004; Crosta *et al.*, 2009a; Poschinger and Kippel, 2009; Iverson *et al.*, 2011; Crosta *et al.*, 2015; Iverson *et al.*, 2015; Collins and Reid, 2020). However, mechanisms resulting in flowslide mobility remain in debate, but some basic information is relatively clear. These studies showed that the catastrophic flowslides commonly occur a transformation from slide to flow. Furthermore, the transformed progress generally involves an undrained loading by overlying landslide mass, which is more prevalent in granular materials, such as sand, silt, and debris, along the flow path (Hutchinson and Bhandari, 1971; Wang *et al.*, 2003; Sassa and Wang, 2005). The liquefaction of the granular materials is crucial to maintain rapid and long-runout landside mobility (Hutchinson and Bhandari, 1971; Evans *et al.*, 2001; Take and Beddoe, 2014). Furthermore, the liquefied substrates have been considered vital to the transformed landslide mobility (Iverson *et al.*, 1997; Wang *et al.*, 2003; Iverson *et al.*, 2011). Nevertheless, Mangeney

(2011) argued that flow-like mobility could also occur in completely dry granular materials due to the lack of cohesion. Essentially, the mobility depends finally on the frictional or rheologic behaviors of sheared granular materials. Additionally, the transformation progress occurs in a channeling flow path, but also on a nearly flat surface. The former has been the focus of considerable research effort in recent years. In comparison, only few studies examined the transformation during movement from steep upper regions onto very flat slopes, focusing on the base liquefaction of the flat flow path (Hutchinson and Bhandari, 1971; Take and Beddoe, 2014; Crosta *et al.*, 2015). The 2014 Oso landslide obtained widespread attention to the catastrophic long-runout mobility on a nearly flat surface, due to the apparent presence of a liquified substrate (Iverson *et al.*, 2015; Iverson and George, 2016; Wartman *et al.*, 2016; Aaron *et al.*, 2017; Stark *et al.*, 2017; Collins and Reid, 2020). However, understanding the mobility of the flowslide on a nearly flat surface remains unclear, as evidenced by the broad range of hypotheses proposed to explain the well-studied Oso landslide's mobility.

Loess flowslides are among the most common of the flow-like landslides, as loess is prone to liquefaction under even an unsaturated condition. Earthquake and rainfall, along with irrigation, have become familiar triggers of the catastrophic loess flowslides in China. Earthquake-induced loess flowslides generally have long-runout mobility if shallow groundwater conditions are present, resulting in liquefied loess with high pore-water pressure and low shear resistance (Ishihara et *al.*, 1990; Wang *et al.*, 2014). Currently, rainfall and irrigation become more frequent triggers to the loess flowslides.

Many studies showed that infiltrated water elevates the groundwater, and cause the loess liquefaction forming the loess flowslides (Derbyshire *et al.*, 2000; Zhang *et al.*, 2014; Zhuang and Peng, 2014; Peng *et al.*, 2015; Peng *et al.*, 2017a; Peng *et al.*, 2017b; Zhang *et al.*, 2017; Zhang and Wang, 2018; Peng *et al.*, 2019). Visibly, water plays a dominant role in the occurrence of the loess flowslides. These studies mentioned above significantly improved our understanding of loess flowslides. Still, much of this effort has been in their initiation and failure mechanisms, examining the liquefied behavior of the loess. Some studies of the mobility of the loess flowslides focused on numerical simulation and field evidence (Peng *et al.*, 2015; Zhang *et al.*, 2017; Kang *et al.*, 2018; Li *et al.*, 2019). Yet there still remains an urgent problem to understand the mobilized mechanisms of a landslide from a slide on the steep upper slope that transforms into a flow on a nearly flat terrace. Such slides frequently threatened the residents and their properties, and also cause major ecological and environmental problems.

This study aims to provide an improved understanding of the transformed mechanism from slide to flow overridden on a liquified substrate. We study a catastrophic flowlside, i.e., the Saleshan landslide of Gansu in China, which killed . We produced geomorphologic and topographic maps for analyzing the movement features of the landslide using cartographic and GIS techniques. We performed electrical resistivity tomography (ERT) to detect groundwater conditions on the landslide body and the terrace. Furthermore, we examined the particle size distributions and triaxial shear behaviors of loess, red soil, and alluvial sand from the landslide deposited zones. We especially performed two loading impact tests on the alluvial sand specimens under drained and undrained status. Finally, we discussed the transformed mechanism of this kind of landslide from slide on steep slopes to flow on gentle terraces, and compare the difference in the liquified entrainment occurred in a steep channel bed erosion along its flow path. Our findings afford some fundamental knowledge to the mobility of this kind of flowslides overridden on a liquefied substrate, and specific assistances for landslide hazard mitigation and risk assessment.

2. Saleshan landslide background

The Saleshan landslide is situated in Dongxiang County, Gansu Province, China (Fig. 1a), and occurred on an afternoon at about 5:46 local time on 7 March 1983, which caused 237 deaths and damage of the four villages. Hence, the Saleshan landslide is among the most disastrous one in the Baxie River catchment, which has hundreds of different types of loess landslides at various sizes (Fig. 1b). Following the updated Varnes landslide classification system, Hungr *et al.* (2014) described the Saleshan landslide as a flowslide, which is characterized by long runout distance traveled across a nearly flat surface. Fig. 1 c and d present the panoramic views of the Saleshan landslide in 1983 and 2015.

2.1 Geological structures

Fig. 2 shows the simplified stratigraphic and topographic section through the pre-landslide topography and the Saleshan landslide along its main sliding direction. The presented stratigraphic and topographic section is revised to the previous version from Zhang and Wang (1984) and Zhang *et al.* (2002). The geological structures can be referred to in the previous studies (Zhang and Wang, 1984; Zhang *et al.*, 2002).

To geological structures before failure (Fig. 2a), the stratigraphic section of the Saleshan landslide include in descending order: (1) Late Pleistocene Lishi Loess (Q_2), (2) Middle Pleistocene Malan Loess (Q_3), (3) Pliocene mudstone and Cobblestone (N_2), (4) Quaternary alluvial sand and gravel, colluvial mudstone and loess (Q_4). The alluvial sand and gravel is located on the first terrace. Moreover, the previous studies speculated that the colluvial mudstone and loess is the deposition of a historical landslide situated over the first terrace (Kang *et al.*, 2018). There are no folds and faults in Saleshan landslide area, which exhibits a simple geologic structure (Zhang *et al.*, 2002). Nevertheless, there are two sets of dominant joints, in which the east-west set is matched with cracks in the main scarp of Saleshan landslide (Zhang *et al.*, 2002).

To geological structures after failure (Fig. 2b), a simplified stratigraphic section can be described as follow: (1) the displaced material of landslide body covered over the alluvial sand and gravel on the first terrace; and (2) the alluvial layer overlies the undisturbed mudstone bedrock. Zhang *et al.* (2002) considered that the alluvial sand and gravel is undisturbed on the first terrace, while other authors argued that the landslide ploughed or impacted the alluvial layer, leading to erosional liquefaction of the substrate (Wang *et al.*, 1988; Kang *et al.*, 2018). It is interesting to note the life-saving tree on the landslide. When the Saleshan landslide occurred, a person tightly held the tree, moving about 960 m without any injures (Zhang *et al.*, 2002; Kang *et al.*, 2018).

2.1 Geomorphologic characteristics

The Saleshan landslide is located on the south facing side of a steep slope ridge on the northern side of Baxie River. The geomorphologic characteristic change of the Saleshan landslide mainly depends on the Baxie River terraces (Fig. 2). The elevation of the Saleshan landslide ranges from 1950 m to 2280 m, including four terraces with abrupt slope angle change. The top of the slope ridge is 2280 m elevation above the fourth terrace, where the slope angle is larger than 50°. The fourth terrace is located between 2195 m and 2080 m elevation, with a slope angle varying from 30° to 35°. The third and second terraces have developed two gentle platforms, and their elevation varies from 2080 m to 1970 m with a switched deep slope with an average 30° slope angle. The lowest first terrace is about 800 m away from the toe of the Saleshan slope with nearly flat surface topography before slope failure. After the Saleshan slope failure, the first terrace became the main accumulation zone. The topographic change reveals that the Saleshan landslide failed from a deep upslope and moved on a flat surface with easy liquified sand and gravel layer, which means an abrupt transformation of movement style. This also indicates that the geologic structure and geomorphologic characteristics is basic conditions for the long-runout mobility during Saleshan landslide propagation.

2.3 Hydroclimatic conditions

The Baxie River basin is a semiarid climate environment. Commonly, the average annual precipitation is 485 mm, with 80% of the total in the period from June to September, and frequent rainstorms in summer (Zhang *et al.*, 2002; Kang *et al.*, 2018). However, the climate presents a wetter environment since 1979, with annual precipitation of 650 mm, and the winter precipitation in 1982 was also above average reaching 66.3 mm (Zhang *et al.*, 2002). There has meltwater before failure in March 1983. Thus, the freeze-thaw effect was suggested to trigger the Saleshan landslide (Huang, 2009). However, Kang *et al.* (2018) considered that the meltwater effectively elevated groundwater, which would be attributed to progressive failure.

The groundwater is of phreatic water, which has all distributed below the fourth terrace (Ma and Qian, 1998). Many springs overflow from the toe of the terraces on both sides of the River valley. Notably, the shallow aquifer on the first terrace is known from borehole information, and the depth of the groundwater table is about 2 m below the ground surface (Ma and Qian, 1998). Besides, the storage water in the Jiuer reservoir was used to the agricultural irrigation on the terraces, guaranteeing the long-term shallow groundwater level. The groundwater information provides useful help to understand the mobility of the Saleshan landslide.

Notably, no observed earthquake and rainfall was recorded in the Baxie River basin in March 1983. Therefore long-term accumulated precipitation and irrigation, rather than abrupt seismic shaking and rainfall infiltration, likely played a key role in initiating the Saleshan landslide.

3. Materials and methods

3.1 Geomorphological features mapping

The geomorphological mapping provides geomorphologic characteristics as an important aid for understanding the inherent problems on the propagation of the landslide. For this purpose, we collected various data from old photos, field investigations, remote images, previous references about Selanshan landslide, and produced a graphical map of geomorphologic imprints using cartographic and GIS techniques. The geomorphological map in this study is representative of many results both from various published data and unpublished reports.

3.2 Topographic changes detection

The topographic change detection is a fundamental prerequisite for landslide deposition thickness but also can provide a direct result assessment for landslide numerical modeling. In this context, we first prepared two large scale topographic maps at the scale of 1:10000 from before and after slope failure, and digitized the two maps using ArcGIS software, and then constructed their digital elevation models (DEMs). After which, we compared and analyzed the topographic change using the Geomorphic Change Detection (GCD) 7.0 software (http://gcd.riverscapes.xyz/), which is a powerful tool on geomorphological change detection (Wheaton *et al.*, 2010; Wheaton *et al.*, 2015). The GCD produced DEM of Difference (DoD) maps before and after the Saleshan landslide, and estimated the net change in geomorphologic features, such as elevation, volume, area.

3.3 Movement features analysis

To analyze mobility after slope failure, we produce a map of movement features, including motion displacement, motion direction, and motion velocity. The motion displacement derives a direct estimate from the placemarks on landslide body, including the sites from house and tree before and after failure. We also record the motion direction of all the placemarks referred to the previous research results (Wang *et al.*, 1988). We also calculated the motion velocity from displacement over time at different sites of the Saleshan landslide. The mobility time derives from seismic signals induced by Saleshan landslide at three seismic stations. The detailed procedure can refer to the supplementary, involving how to digitize old analog seismograms to obtain the relatively accurate time using a MATLAB™ toolbox of DigitSeis developed by Bogiatzis (2015), with slight help of manual processing, to revitalize only three NS analog seismograms from the three seismic stations (Supplementary note, Figs. 1 and 2).

3.4 Textural and mechanical properties test

To obtain the textural and mechanical properties, we taken disturbed loess and red soil (product of mudstone) specimens close to the scarp of the Saleshan landslide, as well as an alluvial sand specimen on the first terrace of Baxie River. These specimens were oven-dried and disaggregated using a rubber hammer. We analyzed particle size distributions of all the samples using a Microtrac S3500 laser diffraction instrument.

Each specimen tested eight times for consistency.

We conducted a series of consolidated undrained compression (CUC) triaxial tests on all the three samples, and two quasi-dynamic impact stress loading (QSL) drained and undrained triaxial tests on the alluvial sand samples. All the specimens have a height of 10 cm and a diameter of 5 cm. All the examples were saturated by carbon dioxide replacement, de-aired water flushing, and back pressure saturation. The specimens were consolidated under a specified cell pressure and then compressed under undrained conditions by means of the strain-controlled method. The axial strain was increased at a rate of 0.01% per minute. The specimens were consolidated and tested at cell pressures of 100, 200, 300 kPa. In CUC sets, compression at each cell pressure was terminated when the axial strain close to 20%. In QSL sets, the specimens were compressed by utilizing a sinusoidal stress loading module, but in which we used a quarter loading period to load 160 kPa with 10 seconds at cell pressures of 200 kPa. Notably, if the stress loading velocity is too rapid, this maybe generates a damage to the triaxial apparatus. We performed one drained stress loading test, and other for the undrained condition.

3.5 Electrical resistivity survey

To prospect the internal structure and hydrological environment of the Saleshan landslide, we carried out four electrical resistivity tomography (ERT) profiles (see their locations in Fig. 5) to obtain a detailed characterization about the electrical signals in the first tens of meters below the ground surface. During the field survey, we used a multielectrode system with 120 electrodes both in Wenner-Schlumberger and Wenner arrays with an electrode spacing of 5 m. We located these electrical profiles using a GPS and measured their topographic changes using a laser measuring technique. Finally, we inverted the apparent resistivity data by a tomographic inversion technique using the newest RES2DINV software. During the inversion, we implemented a smoothness-type regularization constrained least squares by using incomplete Gauss-Newton optimization technique, taking the topographical changes into account along the profiles. The optimization technique is to iteratively adjust the resistivity to obtain a minimal difference between the calculated and measured apparent resistivity values. The absolute acceptable error provides a measurement of this difference.

4. Results

4.1 Geomorphologic imprints

The geomorphologic imprints on a landslide provide direct observation and object analysis for dynamic features at different zones, but is important base to hazard management land planning after the landslide. Fig. 3 shows the geomorphological map of Saleshan landslide, which is a revised version based on the previous conclusions (Zhang *et al.*, 2002; Wu and Wang, 2006). Our geomorphological map presents an immediate and complete description of remaining features at different locations throughout the landslide. From the viewpoint of space elements, we divide the geomorphologic features into three styles. The dotted imprints only have spring outcrop places. The linear features include zone boundaries, major and minor scarps, various cracks, groundwater drainage, and surface water recharge. The planar features involve depressions and hillocks in the zone of depletion, and grooves and hummocks in the zone of accumulation, along with river gully and reservoir adjacent landslide.

There are several critical features worth analyzing. First, the different types of cracks portray the deformation behaviors at respective locations. The cracks distributed on the crown portray tensile deformation, and the lateral and transverse cracks that occurred on the flank signify tractive deformation and fracturing process. These radial cracks emerge thrust behavior on the toe. The depressions and hillocks underwent extension and compression during the landslide movement. The significant number of hummocks on the zone of accumulation show the evidence of fluidization and extension during landslide mobility. There are more in the west-slide and central regions than in the east slide in the zone of accumulation. Using hummocks that explain the motion behavior of the fluidized landslides has also been paid special attention by other authors (Paguican *et al.*, 2014; Collins and Reid, 2020; Dufresne and Geertsema, 2020). The hummocks on a landslide can reveal important movement features during their motion.

Fig. 4 shows the old photographs illustrating typical geomorphological imprints of the Saleshan landslide. These photographs were taken shortly after the landslide in 1983. They not only well verify the evidence from the geomorphological map (Fig. 3), but some of them provide more intuitive clues to uncover movement behavior. As shown in Figs. 4c and 4d, the standing cow and life-saving tree reveal that the displaced materials were incompletely disturbed, mainly maintaining the original stratigraphic structure. Thus, we can speculate that the landslide body moved along a slip surface with low shear resistance. Also, we observe differential movement on the zone of accumulation, due to differences in disturbance and liquefaction of the displaced materials (Fig. 4i-Fig. 4l). The loess at right flank is completely liquified (Fig. 4i), and the deposit at the toe dammed the Baxie River gully with high water content (Fig. 4j). While the deposit close to left flank buried the Jiuer reservoir (Fig. 4k), but they hold some original structures presenting a low water content context.

From the geomorphologic imprints and evidence, we suggest that the Saleshan landslide exists a motion transformation from slide to flow and that the flow-like materials failed along a week slip surface with some differences in deposit features. Meanwhile, this evidence affords clues to analyze the characteristics of accumulation and mobility after slope failure.

4.2 Topographic changes

There are few accurate measurements of the volume of a historical landslide, because of a difficulty gaining the pre- and post-landslide topographic data. Fig. 5a shows the elevation difference of the pre- and post-landslide on the Saleshan landslide. Fig 5b and 5c show geomorphic change detection, the areal and volumetric elevation change distributions. The negative elevation is for erosion, and positive elevation is for accumulation, respectively. The elevation change range of erosion area is −142 to 0 m, which located on the depletion zone. The elevation change range of accumulation distributes between 0 and 39 m occurred in the accumulation zone. Volume proportions of erosion and accumulation are almost the same, which are 55.69 and 44.31%, respectively. The decrease of accumulation volume may be due to the part of loess flowing into Baxie river and Jieer reservoir. The areal proportion of erosion (35.11%) is about half as much as deposition (64.89%).

To better detect the dynamic process of landslides, such as the change of area, volume, and elevation in pre- and post-landslide, we used the Geomorphic Change Detection (GCD) 7.0 software to construct seven two-dimensional profiles of the slip surface in the movement direction and four profiles perpendicular to the movement direction (Fig. 5a). By analyzing the profiles (Fig. 6), we can further understand the characteristics of the topographic change of the Saleshan landslide. With steeper slopes, the erosion probability is higher, and the maximum erosion height up to 139 meters, while the majority of accumulation occurs on the flat areas (P1-P7). It also can be found that erosion mainly occurs on the fourth terrace, and the first terrace is the accumulation zone. The accumulation and erosion features are related to the evidence from geomorphologic characteristics. For the four profiles perpendicular to the movement direction, the degree of erosion at area of P8 and P9 is much greater than that of P10 and P11. As P8 and P9 is located at the trailing edge of the landslide, others are at the leading edge of the landslide. Likewise, hillocks and scarps at the trailing edge of the landslides are eroded, while gullies are piled up and filled. These profiles describe the exterior morphological features and structures in the horizontal and vertical directions, and it can highlight some changes in pre- and post-landslide.

4.3 Rapid and long-runout mobility

In the mobility of the rapid and long-runout landslides, its velocity, displacement, and direction are vital kinematic parameters. Nevertheless, they are often uncertain because this is practically difficult to identify the kinematic parameters accurately. However, the surviving placemarks, e.g., tree and house, could be useful in the dynamic analysis. Fig. 7 shows the motion displacement vector at different placemark locations on the Saleshan landslide, and the calculated kinematic parameters are listed in Table 1. Among these placemarks, there is the most significant motion displacement of 1090 m and the highest motions velocity of 19.8 m/s. The results reveal that the Saleshan landslide underwent rapid and long-runout mobility, in which appeared apparent variable zonation of motion.

On the depletion zone, the three placemarks are almost the same with the horizontal displacements from 310 to 340 m, which means that the vertical fall is significant in the zone (see Fig. 1b). There has the lowest average velocity of 5.9 m/s in the whole landslide zones with a velocity between 5.8 and 6.2 m/s. Due to the calculated velocities on the total mobilized time of 55 seconds, the velocity of the depletion zone may severely be underestimated in the three placemarks. The previous dynamic studies and eyewitness account showed that the velocity of the sliding blocks both exceeds 20 m/s in the depletion zone (Miao *et al.*, 2001; Zhang *et al.*, 2002; Kang *et al.*, 2018).

On the accumulation zone, the displacement vectors present distinct kinematic differences. The placemarks of the central accumulation zone have the greatest motion displacement with the highest landslide velocities. There have relatively more significant displacement and velocity on the west accumulation zone than on the east accumulation zone. It should be noted that there have relatively low velocity and small motion displacement closer to both the flanks. It is consistent with the field evidence (Fig. 4k). This means that the displaced materials immediately stop after rupturing the slide surface. In addition, the motion directions of the various placemarks depend on the original topographic changes and geomorphologic features (Fig. 3 and Fig. 4).

In sum, the Saleshan landslide was rapid in the progress of long-distance motion. The motion of Saleshan landslide primarily occurred on the accumulation zone, in which the velocity and displacement of the displaced materials decrease from the central zone to two flanks. The motion features are matched with the evidence from geomorphologic maps and topographic changes (Fig. 3~Fig. 6). Besides, the underestimated velocity derived from displacement and time may result in some misleading to kinematic analysis.

4.4 Structural and hydrological constraints

ERT is widely used in landslide investigation characterized by a complex geological setting (Perrone *et al.*, 2014). And recently time-lapse ERT is increasingly applied in long-term landslide monitoring (Grandjean *et al.*, 2011; Chambers *et al.*, 2013; Wilkinson *et al.*, 2016; Crawford *et al.*, 2019). Thus, ERT used as a conventional geophysical prospecting method to the geological structure and hydrological environment of a landslide, now becomes a convenient technology using in-situ landslide monitoring.

Fig. 8 shows the interpreted Wenner ERT sections of four profiles on the Saleshan landslide, and the detailed location of the four profiles are shown in the index figure and Fig. 6. The profile L1 is longitudinal through the front zone of depletion, and the end zone of accumulation along movement direction (Fig. 8a), and the profile C1 is transverse through the toe region of rupture surface (Fig. 8b). In addition, the interpreted Wenner Schlumberger ERT sections of four profiles are shown in Supplementary Figs 3. The profiles L1 and C2 profiles orthogonally cross through the middle zone of accumulation on the first terrace (Fig. 8c and d). In the profile L1, the high resistivity sections correspond with the front zone of depletion with relatively low water content and complete structure, while the end zone of accumulation presents low resistivity. The information disclosed from ERT image is matched with the data of borehole after the landslide (Wu and Wang, 2006), along with in-situ investigation. Notably, there is an abundant phreatic region around the rupture surface. It can be verified the evidence from the spring exposed on the third and fourth terrace, along with the surface water convergence in the gully (See Fig. 3). The low resistivity in the profile C1 is consistent with the gully sites, where there has high water content in lowland causing thinker deposit and greater mobility (See Fig. 6). Meanwhile, the toe zone of the rupture surface has relatively lower resistivity, comparing with the zone of depletion. The information from profiles L1 and C2 shows that the displaced materials thickness vary between 15 and 20 m, and that they deposited on the original ground surface (Fig. 6). The deposit is thinner closer to the tip of the Saleshan landslide.

Notably, the sediments below the farmland ground exert a very low resistivity signifying a high water content condition. This is well-matched with direct field observations after the landslide, such as loess liquefaction and deposit with high water content (see Fig 4j and Fig 4l) on the west zone of accumulation.

The electrical resistivity could obtain useful geophysical signals varying with the nature and state of granular materials, as well as the fluid in the granular medium. Thus, the four ERT survey images add information on the internal structure of the Saleshan landslide, which is consistent with the geomorphologic features and topographic changes. Meanwhile, the ERT images well provide the hydrological information, which helps the understanding of the propagation of the Saleshan landslide.

4.5 Liquefaction behaviors

4.5.1 Particle size distribution

The particle size distributions are often crucial for appraising liquefaction potential of flow slides (Kramer, 1988; Picarelli, 2010), and could be indirectly used to interpret liquefaction behaviors of fine granular soils. Fig. 9 shows the exemplified particle size distribution of the three types of soil on the Saleshan landslides. To facilitate a much clearer view of particle size, Fig. 9b uses a linear abscissa, rather than a logarithmic abscissa. Other repeated test results were shown in Supplementary Figs. 4. The three samples are silty soils with uniform gradation. The loess has the greatest fine fractions, and the alluvial sands include the coarsest fractions, whereas the red soil is intermediate. Note that there are two modes on the frequency curves with two unimodal curves and one bimodal curve. The loess and red soil have both a smooth unimodal frequency distribution curve. The loess has a single fine component with a size boundary of 20-60 μm and mean practice size (D_{50}) of 38 μm. The texture of the red soil is like that of the loess, but it has a deviation with a size range of 25-55 μm, and a mean practice size of 43 μm. This kind of deviation may derive from the modification of weathering processes of mudstone. The alluvial sand has a bimodal frequency distribution of particle size, and the range is from 25 μm to 60 μm with a mean practice size of 48 μm. Generally, the bimodal sand is a typical production of a modern alluvial or fluvial environment (Taira and Scholle, 1979; Sun *et al.*, 2002). Compared to evidence from the particle size distribution in other flowslides (Kramer, 1988; Picarelli, 2010; Zhang *et al.*, 2019), all the three samples on the Saleshan landslide are characteristic of liquefaction features, which have the potential to liquefy when close to saturation.

4.5.2 Shear properties

It is still necessary to examine the shear properties of soil to understand its liquefaction behaviors directly. Fig. 10 compares the results of the undrained triaxial shear tests of the three soils on the Saleshan landslide at the same confining pressure (i.e., 200 kPa). Fig. 10a and b present the change deviator stress and pore water pressure with axial strain. Fig. 10c depicts an effective stress path. The three specimens have apparent differences in liquefication behaviors. The loess specimen shows a typical strain behavior maintaining high pore water pressure with an obvious decrease in strength after peak value. The results are consistent with those observed in the liquified or collapsed loess elsewhere (Zhang *et al.*, 2013; Wang *et al.*, 2014; Zhang *et al.*, 2014; Zhang and Wang, 2018). This means that the loess in Saleshan landslide area has visible liquefaction behavior under undrained condition, which is matched with in-situ evidence (Fig. 4i). Notably, the red soil has the lowest liquefaction potential with very light strength decrease after peak strength, although its particle size distribution is located between loess and alluvial sand. It may be related to the strong cementation or bonding existing in the weathering products of mudstone, which could attribute to more clay fractions in the red soil. The alluvial sand specimen has the most significant increase in pore water pressure after the peak strength. As shown in Fig. 9, the alluvial sand is comprised of fine sand, and finer suspended muddy. The small amount of suspended muddy slightly decreases the liquefication of the alluvial sand. Similar results have been found in ring shear and triaxial shear tests (Wang *et al.*, 2007; Carraro *et al.*, 2009).

Fig. 11 shows the undrained triaxial test results for the alluvial sand specimens. The deviator stress of all the specimens increases a peak value with increasing axial strain; after that, abruptly decreases a steady-state with further increase in axial strain (Fig. 11a). Meanwhile, the pore water pressure continuously increases to a steady value with increasing axial strain (Fig. 11b). The effective stress paths show that pure contractive behavior during undrained compression shearing (Fig. 11c). These results further support that all the alluvial sand specimens present unusual liquefaction behavior, and that is more prominent at low confining pressure.

Fig. 12 shows the triaxial test results from quasi-dynamic impact stress loading of the alluvial sand specimens under drained and undrained conditions. In the drained condition, the pore water pressure increases rapidly to 20 kPa in the progress of the impact loading (i.e., 10s), and after that, it has an obvious decrease with almost constant loading deviatoric stress of 160 kPa (Fig. 12a). Meanwhile, the generated pore water pressure dissipated gradually with 100 s. The relatively high dissipation rate in pore water pressure could be attributed to its inherent granular characteristics (Fig.9). This is in contrast to the behavior exhibited in undrained impact loading, and the pore water pressure is the same rapid increase as the drained impact stress loading (Fig. 12b). The desired impact stress could not fully load on the samples, and it has completely collapsed with a rapid increase in pore water pressure. After that, the pore water pressure slightly increases and, accordingly, a striking decrease in deviatoric stress. It is essential for a structural collapse with a great axial displacement. The results show that impact can generate pore water pressure on the alluvial sand, and the undrained impact loading is easier to produce pore water pressure on the alluvial sand than under drained conditions. Meanwhile, the quickly dissipated pore water pressure on the alluvial sand may contribute to the liquefaction of the loess, and consequently enhanced the mobility of the Saleshan landslide. This finding is consistent with those research results from ring shear tests (Wang *et al.*, 2003) and numerical simulation (Collins and Reid, 2020).

4. Discussion

4.1 Transformation from a slide on the steep slope to flow on the gentle terrace

The Saleshan landslide experienced a typical transformation from progressive slide to catastrophic flow, i.e., velocity transition from slow to fast. The progressive deformation along a sliding surface went through more than four years from the evidence of monitoring data and eyewitness account, while the disastrous mobility after failure initiation only underwent 60 seconds with about 1000 m mobility (Wang *et al.*, 1988; Miao *et al.*, 2001; Zhang *et al.*, 2002; Wu and Wang, 2006; Kang *et al.*, 2018). Fig. 13 shows the hypothesized sequence from progressive deformation to the catastrophic mobility of 1983 Saleshan landslide. The stage from slow to accelerated deformation resulted in the pore water pressure accumulation in the toe zone of the slope (Fig. 13a and b). After that, the landslides on dissected steep mudstone slope transformed into a flow-type landslide that travels long runout distance across a nearly flat terrace (Fig. 13c). Finally, the elevated reservoir water triggered landslide dam-break (Fig. 13d). The previous studies have well analyzed the deformation mechanism of the Saleshan landslide, but the unexpected flow-type mobility remains unclear. Thus, we focus here on the transformation mechanisms from the slide on steep upper slope to flow on nearly flat terrace.

The transformed landslide from slide to flow could be attributed to the unusual structural and hydrological configurations of the toe and travel zone of the Saleshan landslide. There is enough surface and sub-surface water convergence, leading to a shallow groundwater level in alluvial sand layers with high liquefaction potential on the first terrace. The evidence can prove the speculation from geomorphologic mapping (Figs 2 and 3), ERT survey (Fig 8), and test results (Figs. 9-11). Generally, the groundwater condition is key to the transformation from progressive slide to catastrophic flow in the Saleshan landslide; meanwhile, the highly susceptible to liquefaction alluvial sand is essential to the transformation. On the whole, the transformation strictly depends on the liquefied substrate, i.e., alluvial saturated or even partly saturated sand layer on the first terrace. Of course, as revealed by results in field and laboratory (Figs. 3-5 and Fig. 10), the highly liquefied loess has a particular contribution to the mobility after failure.

In the Chinese Loess Plateau, identical loess flowslides have frequently occurred on the Jingyang platform (Xu *et al.*, 2009; Peng *et al.*, 2017a; Peng *et al.*, 2018; Li *et al.*, 2019). These researchers also proved that the hydrogeological conditions on the nearly flat river terrace close to the current Wei River, i.e., the alluvial sand layer and high groundwater level, control the transformed progress. Incorporating with evidences from liquefied sand pipes observed in loess deposits (Xu *et al.*, 2009) deduced a conceptualized liquefaction model in double layers (i.e., sand and loess) along sliding surface on the nearly flat terrace. Peng *et al.* (2018) excavated several big exploratory trenches on the accumulation of the flowslides, and they found typical liquefied evidence of sand pipes and sand boils intruded into loess deposits. However, it lacks direct ground evidence, which can be attributed to the thick loess deposits with relatively low permeability. Also, the numerical simulation and shear wave detection supported that liquefaction entrainment of the terrace sand deposits controls their rapid and long runout mobility of those loess flowslides (Peng *et al.*, 2017a; Li *et al.*, 2019).

In the rest of the world, there have been similar structural and hydrologic constraints with the above loess flowslides, which resulted in the same transformation from slides on steep upper slope to flows with high mobility on a gentle lower terrace. A famous example in Switzerland is the Flims rockslide avalanche, which liquefied alluvial deposits on the terrace, leading to about 13 km displacement and damming of the Vorderrhein river valley (Poschinger and Kippel, 2009). There was observed the sub-vertical tubes of gravel composition almost without any fines in the landslide deposits (Pavoni, 1968), and these finer materials such as sand and silt have been washed out during water flow (Pavoni, 1968; Poschinger and Kippel, 2009). This is a typical feature of liquefaction of alluvial deposits. The scholars in Czech Republic found that a massive rockslide avalanche transformed as a long-runout landslide along the terrace in the Bilina river (Burda *et al.*, 2018). The data shows that the slope of the terrace is generally lower than 10 degrees in this study region (Poschinger and Kippel, 2009; Burda *et al.*, 2018). In Saskatchewa river, there have many landslides dissected on shale slopes; some of them transformed into a fluidized landslide that mobilized far beyond that expected on a nearly flat terrace. Moreover, multiples boreholes revealed that the sliding surface is located on Tertiary sand in the Hepburn aquifer system (Misfeldt *et al.*, 1991). Thus, enough groundwater and sand prone to liquefaction are essential to these landslides that occurred in the Saskatchewa river region. Crosta *et al.* (2015) presented multiple examples of landslides from steep slopes falling onto a shallow erodible substrate or water layer, and then travel long-runout distance with typical high velocity. Crosta and his colleagues have confirmed that the loading processes of the overlying landslide mass resulted in the substrate liquefaction is key to the mobility on a flat area (Crosta *et al.*, 2009a; Crosta *et al.*, 2009b; Crosta *et al.*, 2015; Crosta *et al.*, 2016). The very recent 2014 Oso landslide gained a lot of attentions about its long runout mobility mechanism. The Oso landslide failed on steep slopes, and then move along a nearly flat terrace (Iverson *et al.*, 2015; Iverson and George, 2016; Wartman *et al.*, 2016; Stark *et al.*, 2017; Collins and Reid, 2020). However, these authors argue about the sequential stages of the Oso landslide and what material was liquefied to explain its long runout mobility on the nearly flat alluvial plain.

The aforementioned typical examples improve our understanding of the transformed landslide from slides on steep upper slopes to flow along gently terrace and provide important insight of the base liquefaction of terrace deposits controlling rapid and long-runout mobility, although disagreement remains regarding mechanisms involved. However, these example landslides confirm that the unusual structural and hydrologic configurations on the slope toe and fronted terrace zones are critical for producing a rapid, long-runout landslide overriding terrace deposits.

4.2 Rapid and long-runout mobility overridden on a liquefied substrate

There should be similar transformed and mobilized mechanisms between Saleshan landslide and these landslides mentioned above. The landslides detected on steep upper slopes transformed into flow-type landslides, causing a rapid and long-runout mobility overridden on the sand substrate on the nearly flat or gentle terrace with enough water. Overall, there can divide into two stages after slope failure. One is the instantaneous transformation of movement style at the toe of the slope; the second is then long-runout mobility on the fronted terrace. They are both attributed to dynamic loading from upper landslide mass on the lower liquefied substrate, which is generally composed of alluvial sand and silt of terrace deposits. And consequentially, the impact loading results in the generation of excess pore water pressure on the liquefied sand at the toe of the terrace deposits under undrained condition, causing a dramatic decrease in shear resistance of the saturated sand. Nevertheless, there has an essential difference during transformation and mobility. The transformed moment should be in an undrained condition with almost constant pore water pressure, along with a lower shear resistance. While the mobilized progress is more like a drained condition with almost constant shear resistance, comparing continuously dissipated pore water pressure. Our triaxial dynamic impact loading provides a reasonable explanation for the hypothesized mechanism to transformation and mobility (Figs. 12). This mechanism is consistent with those obtained in physical and numerical simulations performed by other authors (Take and Beddoe, 2014; Crosta et al., 2016; Collins and Reid, 2020).

It is worth to mention another type of the transformed landslide from slide to flow coupled with a channel bed erosion along its flow paths. In these events, the displaced materials after failure entrain and liquefy saturated soil from its flow paths along the channel on a slope (Evans *et al.*, 2001; Wang *et al.*, 2003; Hungr and Evans, 2004; Iverson *et al.*, 2011). There also had a typical case study in Chinee loess areas, i.e., the Dagou loess flowslide with significant entrainment (Peng *et al.*, 2015; Zhang *et al.*, 2017). The underlying process of entrainment and liquefaction is a rapid undrained loading from the overriding landslide mass. As the dynamic undrained loading leads to an increase in pore water pressure (Hutchinson and Bhandari, 1971; Sassa and Wang, 2005; Wang *et al.*, 2013), and liquefy the underlying deposits on the channel (Wang *et al.*, 2013; Collins and Reid, 2020), causing entrainment of landslide with higher volume and greater mobility (Hungr and Evans, 2004). As the channelizing topography can focus landslide momentum (Iverson *et al.*, 2015), and wet bed deposit can enhance its mobilized capacity (Iverson *et al.*, 2011; Iverson *et al.*, 2015). In the study to the 2014 Oso landslide, however, Iverson *et al.* (2015) pointed out that the transformed landslide into a nearly flat surface is unlike virtually all the flow along the channelling path. This is because, as suggested by Hutchinson and Bhandari (1971), the rapid mobility overridden on a nearly flat slope partakes more of mass transport than the mass movement.

Hence, the transformation from slide to flow includes two modes due to topographic differences. However, there is the same increase in pore water pressure in the liquefied substrate triggered by dynamic loading (Fig. 14). Meanwhile, the transformation of the two movement types is both transients to the generation of pore water pressure in the erosional layer, and the followed long-runout mobility depends on topographic change and dissipated time of the pore water pressure.

5. Conclusions

The flowslide overridden on a liquified substrate generally mobilized on a nearly flat flow path, causing rapid long-runout distance and catastrophic threats. We studied the Saleshan landslide of Gansu in China, which is a typical loess flowslide mobilized on the nearly flat terrace with an easily liquefied alluvial sand substrate. The geomorphologic imprints and topographic changes present the different dynamic features and mobilized behaviors at different zones of the Saleshan landslide. And its accumulated features and the placemarks show that the landslide exists a motion transformation from the slide on the steep slope to flow on the gentle terrace with rapid velocity and long-runout distance. Meanwhile, ERT surveying confirms the existence of abundant groundwater in the accumulation zone of the Saleshan landslide, which is crucial to the motion transformation.

Our triaxial shear tests suggest that loess, alluvial sand, and red soil are sensitive to liquefaction at the undrained conditions. Among them, the loess is the easiest liquefaction. The impact loading test results show that the alluvial sand is natural liquefaction at undrained condition while it is difficult to drained condition due to rapid water pore pressure dissipation. This aggravated the occurrence of the mobilized loess. As a result, the progress enhanced the mobilization of the Saleshan landslide on the nearly flat terrace. Overall, we conclude that the hydrologic condition of the terrace is essential to the movement of the Saleshan landslide, and the liquefaction features of the materials are the key to its transformation during the landslide’s movement. Meanwhile, this kind of flowslide overridden on the liquified substrate partakes more of mass transport than a mass movement.

Acknowledgments

This study was partially supported by the National Natural Science Foundation of China (Nos. 41977212, 41790443 and 41927806), the National Key Research and Development Program of China (No. 2018YFC504702). Mr. Xishan Lin, Mr. Shuaijun Hu, and Mr. Xiaoming Feng of Lanzhou University are thanked for their help in the field investigation. Yao Jiang acknowledges support from the CAS Pioneer Hundred Talents Program. Images of the geographic, topographic, geomorphic maps and photographs used for this paper are properly cited and referenced. Original data from ERT, particle size distribution and triaxial shear test are available upon request (zhangfy@lzu.edu.cn).

References

Aaron, J., Hungr, O., Stark, T.D., Baghdady, A.K., 2017. Oso, Washington, landslide of March 22, 2014: Dynamic analysis. Journal of Geotechnical & Geoenvironmental Engineering 143.

Bogiatzis, P., 2015. Revitalizing decades-old analog seismograms through image analysis and digitization. Mathwork, Technical Articles and Newsletters, https://www.mathworks.com/company/newsletters/articles/revitalizing-decades-old-analog-seismograms-through-image-analysis-and-digitization.html?s_tid=srchtitle.

Burda, J., Veselý, M., Řehoř, M., Vilímek, V., 2018. Reconstruction of a large runout landslide in the Krušné hory Mts. (Czech Republic). Landslides 15, 423–437.

Carraro, J.A.H., Prezzi, M., Salgado, R., 2009. Shear strength and stiffness of sands containing plastic or nonplastic fines. Journal of Geotechnical and Geoenvironmental Engineering 135, 1167-1178.

Chambers, J., Meldrum, P., Gunn, D., Wilkinson, P., Merritt, A., Murphy, W., West, J., Kuras, O., Haslam, E., Hobbs, P., 2013. Geophysical-geotechnical sensor networks for landslide monitoring. Landslide Science and Practice. Springer, pp. 289-294.

Collins, B.D., Reid, M.E., 2020. Enhanced landslide mobility by basal liquefaction: The 2014 State Route 530 (Oso), Washington, landslide. GSA Bulletin 132, 451-476.

Crawford, M.M., Bryson, L.S., Woolery, E.W., Wang, Z., 2019. Long-term landslide monitoring using soil-water relationships and electrical data to estimate suction stress. Engineering Geology 251, 146-157.

Crosta, G., Imposimato, S., Roddeman, D., 2009a. Numerical modeling of 2‐D granular step collapse on erodible and nonerodible surface. Journal of Geophysical Research: Earth Surface 114.

Crosta, G.B., Blasio, F.V., Caro, M., Volpi, G., Imposimato, S., Roddeman, D., 2016. Modes of propagation and deposition of granular flows onto an erodible substrate: experimental, analytical, and numerical study. Landslides, 1-22.

Crosta, G.B., Blasio, F.V.D., Locatelli, M., Imposimato, S., Roddeman, D., 2015. Landslides falling onto a shallow erodible substrate or water layer: an experimental and numerical approach. IOP Conference Series: Earth and Environmental Science 26, 012004.

Crosta, G.B., Imposimato, S., Roddeman, D., 2009b. Numerical modelling of entrainment/deposition in rock and debris-avalanches. Engineering Geology 109, 135-145.

Derbyshire, E., Meng, X.M., Dijkstra, T.A., 2000. Landslides in the Thick Loess Terrain of North-West China. Wiley.

Dufresne, A., Geertsema, M., 2020. Rock slide–debris avalanches: flow transformation and hummock formation, examples from British Columbia. Landslides, 1-18.

Evans, S.G., Hungr, O., Clague, J.J., 2001. Dynamics of the 1984 rock avalanche and associated distal debris flow on Mount Cayley, British Columbia, Canada; implications for landslide hazard assessment on dissected volcanoes. Engineering Geology 61, 29-51.

Grandjean, G., Gourry, J.C., Sanchez, O., Bitri, A., Garambois, S., 2011. Structural study of the Ballandaz landslide (French Alps) using geophysical imagery. Journal of Applied Geophysics 75, 531-542.

Huang, R., 2009. Some catastrophic landslides since the twentieth century in the southwest of China. Landslides 6, 69-81.

Hungr, O., Evans, S.G., 2004. Entrainment of debris in rock avalanches: An analysis of a long run-out mechanism. Geological Society of America Bulletin 116, 1240-1252.

Hungr, O., Leroueil, S., Picarelli, L., 2014. The Varnes classification of landslide types, an update. Landslides 11, 167-194.

Hutchinson, J.N., Bhandari, R.K., 1971. Undrained loading, a fundamental mechanism of mudflows and other mass movements. Géotechnique 21, 353-358.

Ishihara, K., Okusa, S., Oyagi, N., Ischuk, A., 1990. Liquefaction-induced flowslide in the collapsible loess deposit in Soviet Tajik. Soils and Foundations 30, 73-89.

Iverson, R.M., George, D.L., 2016. Modelling landslide liquefaction, mobility bifurcation and the dynamics of the 2014 Oso disaster. Géotechnique 66, 175-187.

Iverson, R.M., George, D.L., Allstadt, K., Reid, M.E., Collins, B.D., Vallance, J.W., Schilling, S.P., Godt, J.W., Cannon, C.M., Magirl, C.S., Baum, R.L., Coe, J.A., Schulz, W.H., Bower, J.B., 2015. Landslide mobility and hazards: implications of the 2014 Oso disaster. Earth and Planetary Science Letters 412, 197-208.

Iverson, R.M., Reid, M.E., LaHusen, R.G., 1997. Debris-flow mobilization from landslides. Annual Review of Earth and Planetary Sciences 25, 85-138.

Iverson, R.M., Reid, M.E., Logan, M., LaHusen, R.G., Godt, J.W., Griswold, J.P., 2011. Positive feedback and momentum growth during debris-flow entrainment of wet bed sediment. Nature Geoscience 4, 116-121.

Kang, C., Zhang, F., Pan, F., Peng, J., Wu, W., 2018. Characteristics and dynamic runout analyses of 1983 Saleshan landslide. Engineering Geology 234, 181-195.

Kramer, S.L., 1988. Triggering of liquefaction flow slides in coastal soil deposits. Engineering Geology 26, 17-31.

Li, P., Shen, W., Hou, X., Li, T., 2019. Numerical simulation of the propagation process of a rapid flow-like landslide considering bed entrainment: A case study. Engineering Geology 263, 105287.

Ma, J., Qian, J., 1998. Prediction and evaluation of the influence on environmental hydrogeology in nalesi irrigation district of Baxiehe River Basin. Journal of Lanzhou University 34, 106-111.

Mangeney, A., 2011. Landslide boost from entrainment. Nature Geoscience 4, 77-78.

Miao, T., Liu, Z., Niu, Y., Ma, C., 2001. A sliding block model for the runout prediction of high-speed landslides. Canadian Geotechnical Journal 38, 217-226.

Misfeldt, G.A., Sauer, E.K., Christiansen, E.A., 1991. The Hepburn landslide: an interactive slope-stability and seepage analysis. Canadian Geotechnical Journal 28, 556-573.

Paguican, E.M.R., Wyk de Vries, B., Lagmay, A.M.F., 2014. Hummocks: how they form and how they evolve in rockslide-debris avalanches. Landslides 11, 67-80.

Pavoni, N., 1968. Über die Entstehung der Kiesmassen im Bergsturzgebiet von Bonaduz-Reichenau (Graubünden). Eclogae Geol. Helv 61/2, 494–500.

Peng, D., Xu, Q., Zhang, X., Xing, H., Zhang, S., Kang, K., Qi, X., Ju, Y., Zhao, K., 2019. Hydrological response of loess slopes with reference to widespread landslide events in the Heifangtai terrace, NW China. Journal of Asian Earth Sciences 171, 259-276.

Peng, J., Fan, Z., Wu, D., Zhuang, J., Dai, F., Chen, W., Zhao, C., 2015. Heavy rainfall triggered loess–mudstone landslide and subsequent debris flow in Tianshui, China. Engineering Geology 186, 79-90.

Peng, J., Ma, P., Wang, Q., Zhu, X., Zhang, F., Tong, X., Huang, W., 2018. Interaction between landsliding materials and the underlying erodible bed in a loess flowslide. Engineering Geology 234, 38-49.

Peng, J., Wang, G., Wang, Q., Zhang, F., 2017a. Shear wave velocity imaging of landslide debris deposited on an erodible bed and possible movement mechanism for a loess landslide in Jingyang, Xi'an, China. Landslides 14, 1503-1512.

Peng, J., Zhang, F., Wang, G., 2017b. Rapid loess flow slides in Heifangtai terrace, Gansu, China. Quarterly Journal of Engineering Geology and Hydrogeology 50, 106-110.

Perrone, A., Lapenna, V., Piscitelli, S., 2014. Electrical resistivity tomography technique for landslide investigation: A review. Earth-Science Reviews 135, 65-82.

Picarelli, L., 2010. Discussion on "A rapid loess flowslide triggered by irrigation in China". Landslides 7, 203-205.

Poschinger, A.v., Kippel, T., 2009. Alluvial deposits liquefied by the Flims rock slide. Geomorphology 103, 50-56.

Sassa, K., Wang, G., 2005. Mechanism of landslide-triggered debris flows: Liquefaction phenomena due to the undrained loading of torrent deposits. Debris-flow hazards and related phenomena. Springer, pp. 81-104.

Stark, T.D., Baghdady, A.K., Hungr, O., Aaron, J., 2017. Case Study: Oso, Washington, Landslide of March 22, 2014—Material Properties and Failure Mechanism. Journal of Geotechnical and Geoenvironmental Engineering, 05017001.

Sun, D., Bloemendal, J., Rea, D.K., Vandenberghe, J., Jiang, F., An, Z., Su, R., 2002. Grain-size distribution function of polymodal sediments in hydraulic and aeolian environments, and numerical partitioning of the sedimentary components. Sedimentary Geology 152, 263-277.

Taira, A., Scholle, P.A., 1979. Origin of bimodal sands in some modern environments. Journal of Sedimentary Research 49, 777-786.

Take, W.A., Beddoe, R.A., 2014. Base liquefaction: a mechanism for shear-induced failure of loose granular slopes. Canadian Geotechnical Journal, 496-507.

Wang, G., Huang, R., Chigira, M., Wu, X., Lourenço, S.D.N., 2013. Landslide amplification by liquefaction of runout-path material after the 2008 Wenchuan (M 8·0) Earthquake, China. Earth Surface Processes and Landforms 38, 265-274.

Wang, G., Sassa, K., Fukuoka, H., 2003. Downslope volume enlargement of a debris slide-debris flow in the 1999 Hiroshima, Japan, rainstorm. Engineering Geology 69, 309-330.

Wang, G., Sassa, K., Fukuoka, H., Tada, T., 2007. Experimental study on the shearing behavior of saturated silty soils based on ring-shear tests. Journal of Geotechnical and Geoenvironmental Engineering 133, 319-333.

Wang, G., Zhang, D., Furuya, G., Yang, J., 2014. Pore-pressure generation and fluidization in a loess landslide triggered by the 1920 Haiyuan earthquake, China: A case study. Engineering Geology 174, 36-45.

Wang, S., Zhang, Z., Zhan, Z., Liu, H., 1988. On the characteristics and dynamics of the catastrophic Mount Sale landslide, Gansu. Journal Chengdu College of Geology 15, 58-63.

Wartman, J., Montgomery, D.R., Anderson, S.A., Keaton, J.R., Benoît, J., dela Chapelle, J., Gilbert, R., 2016. The 22 March 2014 Oso landslide, Washington, USA. Geomorphology 253, 275-288.

Wheaton, J.M., Brasington, J., Darby, S.E., Sear, D.A., 2010. Accounting for uncertainty in DEMs from repeat topographic surveys: improved sediment budgets. Earth Surface Processes and Landforms 35, 136-156.

Wheaton, J.M., Fryirs, K.A., Brierley, G., Bangen, S.G., Bouwes, N., O'Brien, G., 2015. Geomorphic mapping and taxonomy of fluvial landforms. Geomorphology 248, 273-295.

Wilkinson, P., Chambers, J., Uhlemann, S., Meldrum, P., Smith, A., Dixon, N., Loke, M.H., 2016. Reconstruction of landslide movements by inversion of 4-D electrical resistivity tomography monitoring data. Geophysical Research Letters 43, 1166-1174.

Wu, W., Wang, N., 2006. Landslide hazards in Gansu. Lanzhou University Press, Gansu, China.

Xu, L., Dai, F., Kwong, A., Tham, L., Tu, X., 2009. Analysis of some special engineering-geological problems of loess landslide. Chinese Journal of Geotechnical Engineering 31, 287-293.

Zhang, F., Kang, C., Chan, D., Zhang, X., Pei, X., Peng, J., 2017. A study of a flowslide with significant entrainment in loess areas in China. Earth Surface Processes and Landforms 42, 2295-2305.

Zhang, F., Wang, G., 2018. Effect of irrigation-induced densification on the post-failure behavior of loess flowslides occurring on the Heifangtai area, Gansu, China. Engineering Geology 236, 111-118.

Zhang, F., Wang, G., Kamai, T., Chen, W., 2014. Effect of pore water chemistry on undrained shear behaviour of saturated loess. Quarterly Journal of Engineering Geology and Hydrogeology 47, 201-210.

Zhang, F., Wang, G., Kamai, T., Chen, W., Zhang, D., Yang, J., 2013. Undrained shear behavior of saturated loess with different concentrations of sodium chlorate solution. Engineering Geology 155, 69-79.

Zhang, F., Yan, B., Feng, X., Lan, H., Kang, C., Lin, X., Zhu, X., Ma, W., 2019. A rapid loess mudflow triggered by the check dam failure in a bulldoze mountain area, Lanzhou, China. Landslides 16, 1981-1992.

Zhang, Z., Chen, S., Tao, L., 2002. 1983 Sale Mountain landslide, Gansu Province, China. Reviews in Engineering Geology 15, 149-164.

Zhang, Z., Wang, S., 1984. On the prediction of the occurrence time and the velocity of a potential landslide. Proceedings, 4th International Symposium on Landslides, Toronto, Canada, pp. 145-146.

Zhuang, J., Peng, J., 2014. A coupled slope cutting—a prolonged rainfall-induced loess landslide: a 17 October 2011 case study. Bulletin of Engineering Geology and the Environment 73, 997-1011.

Figure captions

Fig. 1 Geographical location and reviews of the Saleshan landslide. (a) Location of the Saleshan landslide in Gansu Province, China; (b) Landslide inventory of Baxie River catchment; (c) Panoramic photograph of the Saleshan landslide in 1983 (Courtesy of Y. Wang); (d) Panoramic photograph of the Saleshan landslide in 2015.

Fig. 2 Simplified stratigraphic and topographic section of the Saleshan landslide. (a) Before slope failure; (b) After slope failure.

Fig. 3 Geomorphologic map of Saleshan landslide. 1 Depletion zone; 2 Accumulation zone 3 Depressions; 4 Hillocks; 5 Grooves; 6 Hummocks; 7 Main scarp; 8 Minor scarp; 9 Crown cracks; 10 Lateral cracks; 11 Transverse cracks; 12 Radial cracks; 13 Flanks; 14 Contour lines; 15 Gullies; 16 Springs; 17 Baxie River; 18 Jieer reservoir. The boxes indicate photo locations in Fig. 4, respectively.

Fig. 4 Photographs illustrating typical geomorphological imprints of Saleshan landslide in 1983. (a) Sub-vertical main scarp; (b) Head scarp with depression and hillock; (c) Standing cow in accumulation zone; (d) Life-saving tree at the toe (photo from Zhang *et al.*, 2002); (e) Lateral cracks on the east-side at left flank; (f) Transverse cracks on the west-side at right flank; (g) Transverse cracks on the east-side at left flank; (h) Radial cracks at the toe; (i) Loess liquefaction at right flank on accumulation zone; (j) landslide deposition and dammed lake in Baxie River; (k) Buried Jiuer reservoir and transverse cracks; (l) incompletely liquefied loess on the east-side accumulation zone. See Fig. 3 for photo locations.

Fig. 5 Topographic change detection of pre- and post landslide of the Saleshan landslide. (a) The elevation difference map; (b) the areal change distribution; and (c) the volumetric elevation change distribution. Black lines indicate the profile locations in Fig. 6, and red lines show the profile locations of the ERT surveying in Fig. 8.

Fig. 6 The topographic changes of alternative profiles of the Saleshan landslide, and the specified locations see Fig. 5.

Fig. 7 Motion displacement vector at different placemark locations on the Saleshan landslide. 1 Depletion zone; 2 West accumulation zone; 3 Central accumulation zone; 4 East accumulation zone; 5 House location before failure; 6 House location after failure; 7 Ground marks before failure; 8 Ground marks after failure; 9 Tree location before and after failure; 10 Life-saving tree before and after failure; 11 Placemark number.

Fig. 8 Interpreted Wenner ERT sections of four profiles on the Saleshan landslide. Note: the dashed lines are derived from the real topographic profile, and the detailed locations see Fig. 5 and Fig. 6.

Fig. 9 The exemplified particle size distribution of the three types of soils on the Saleshan landslide. (a) Cumulative distribution curves of particle size; (b) Frequent distribution curves of particle size.

Fig. 10 Undrained triaxial test results of the three different specimens at same confining pressures. (a) Deviator stress versus axial strain; (b) Pore water pressure versus axial strain; (c) Effective stress path

Fig. 11 Undrained triaxial test results of the alluvial sand specimens at different confining pressures. (a) Deviator stress versus axial strain; (b) Pore water pressure versus axial strain; (c) Effective stress path

Fig. 12 Triaxial test results from quasi-dynamic impact stress loading of the alluvial sand specimens. (a) drained impact loading condition; (b) undrained impact loading condition.

Fig. 13 Hypothesised sequence from progressive deformation to the catastrophic mobility of the Saleshan landslide.

Fig. 14 Schematic illustration of two types of entrainment. (a) Mobility overridden on the liquefied substrate on nearly flat flow path; (b) Mobility eroded the liquefied layer in relatively steep channel flow path.

Fig. 1

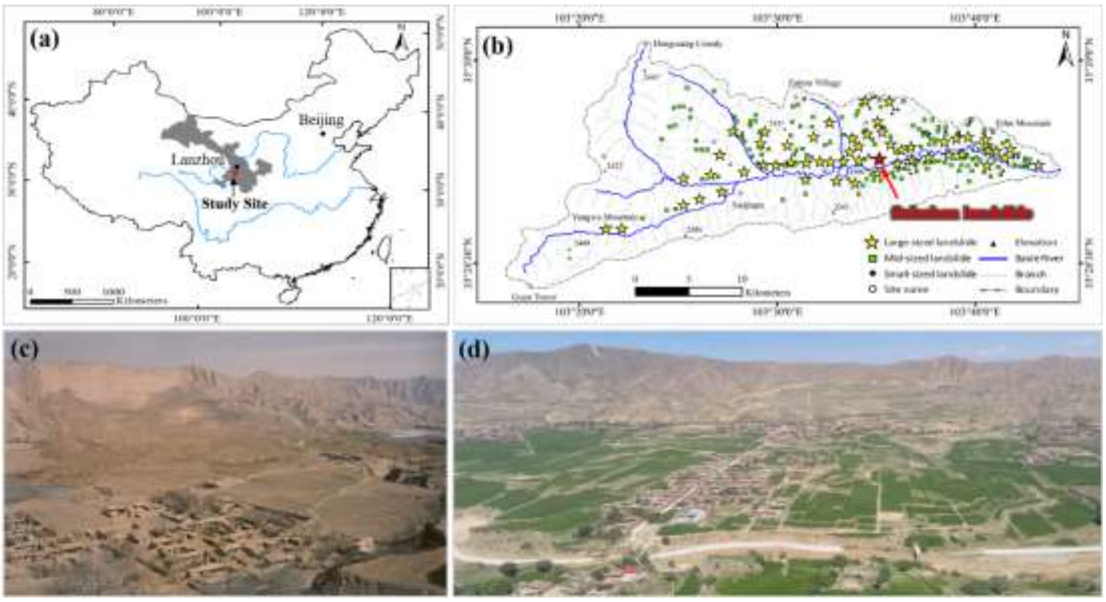

Fig. 2

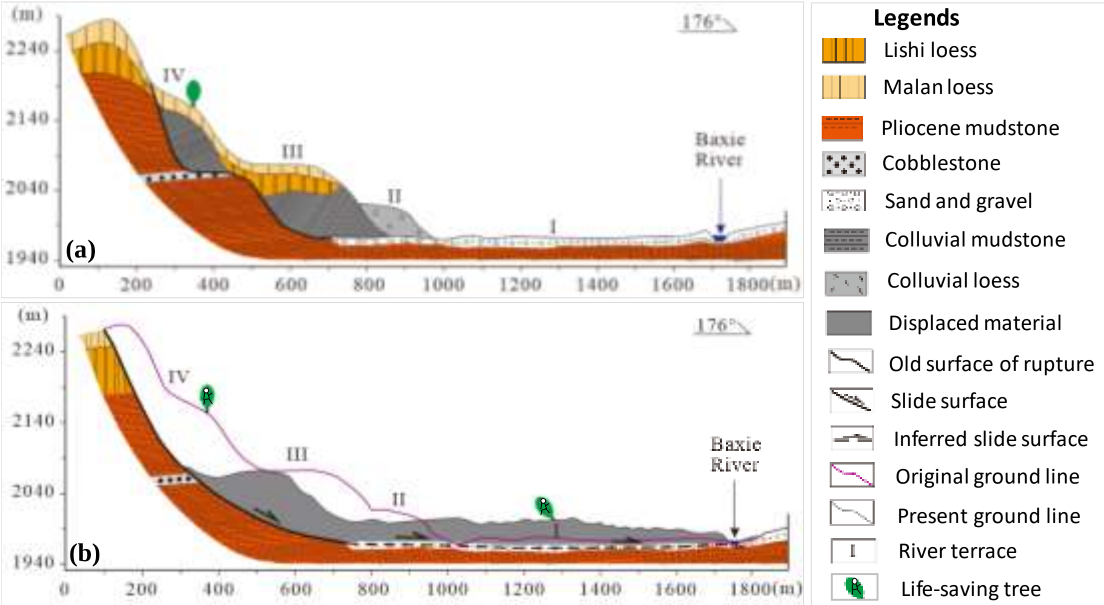
(m)
2240
2140
2040
1940
(a)
0
200
400
600
800
1000
1200
1400
1600
1800(m)
176°
IV
III
II
I
Baxie River
(b)
Legends
Lishi loess
Malan loess
Pliocene mudstone
Cobblestone
Sand and gravel
Colluvial mudstone
Colluvial loess
Displaced material
Old surface of rupture
Slide surface
Inferred slide surface
Original ground line
Present ground line
River terrace
Life-saving tree

Fig. 3

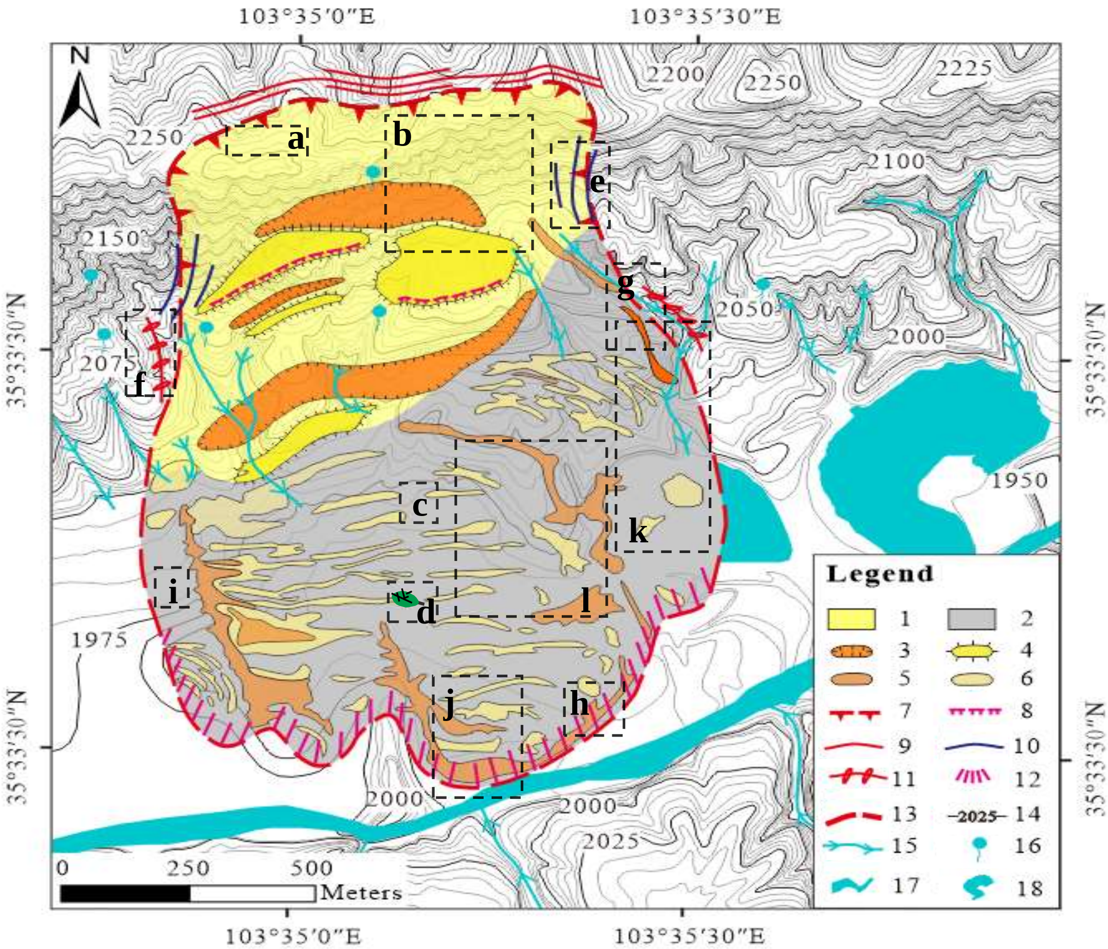

103°35′0″E
103°35′30″E
35°33′30″N
N
2250
2200
2250
2225
2100
2150
2050
2000
1950
1975
2000
2000
2025
a
b
c
d
e
f
g
h
i
j
k
l
0 250 500 Meters
Legend
1
2
3
4
5
6
7
8
9
10
11
12
13
14
15
16
17
18
2025

Fig. 4

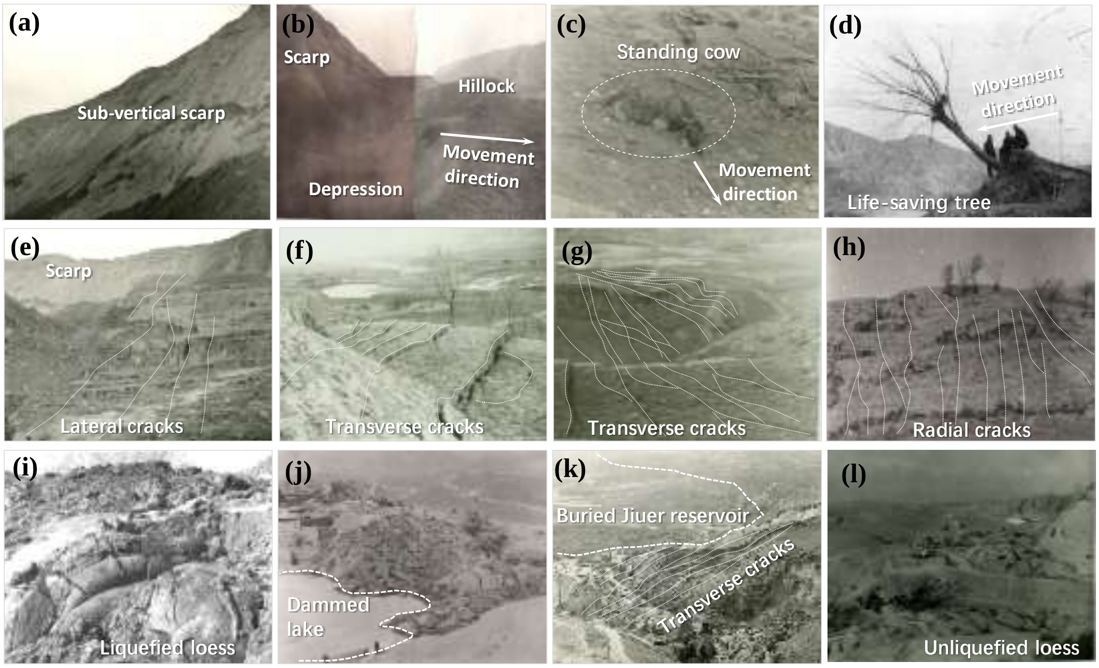
(a)
Sub-vertical scarp
(b)
Scarp
Hillock
Movement direction
Depression
(c)
Standing cow
Movement direction
(d)
Movement direction
Life-saving tree
(e)
Scarp
Lateral cracks
(f)
Transverse cracks
(g)
Transverse cracks
(h)
Radial cracks
(i)
Liquefied loess
(j)
Dammed lake
(k)
Buried Jiuer reservoir
Transverse cracks
(l)
Unliquefied loess

Fig. 5

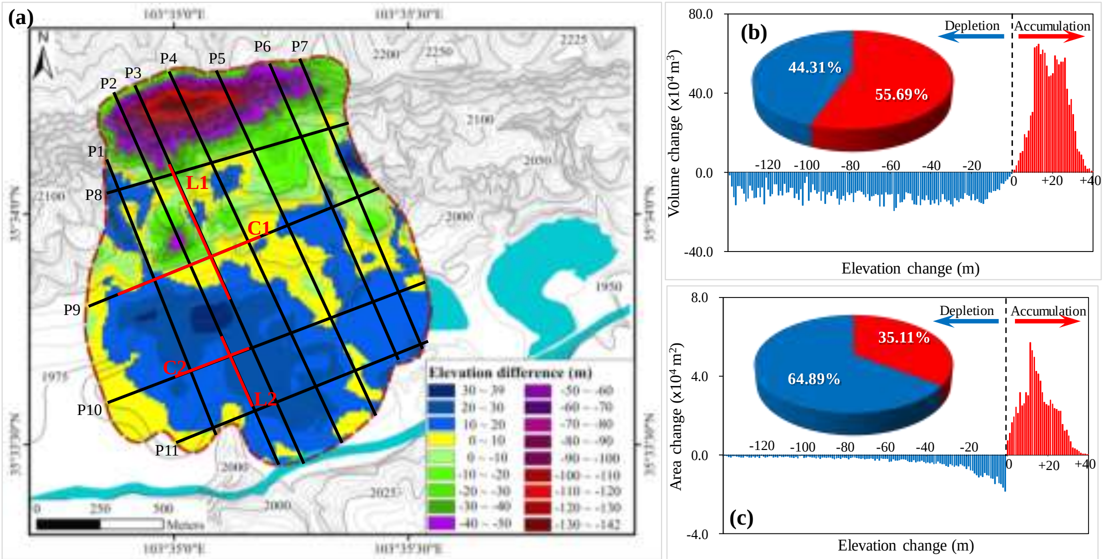
(a)
103°35'0"E
103°35'30"E
P1
P2
P3
P4
P5
P6
P7
P8
P9
P10
P11
L1
L2
C1
C2
Elevation difference (m)
30 ~ 39
20 ~ 30
10 ~ 20
0 ~ 10
0 ~ -10
-10 ~ -20
-20 ~ -30
-30 ~ -40
-40 ~ -50
-50 ~ -60
-60 ~ -70
-70 ~ -80
-80 ~ -90
-90 ~ -100
-100 ~ -110
-110 ~ -120
-120 ~ -130
-130 ~ -142
0 250 500 Meters
(b)
Depletion
Accumulation
44.31%
55.69%
Volume change (x10^4 m^3)
Elevation change (m)
(c)
Depletion
Accumulation
35.11%
64.89%
Area change (x10^4 m^2)
Elevation change (m)

Fig. 6

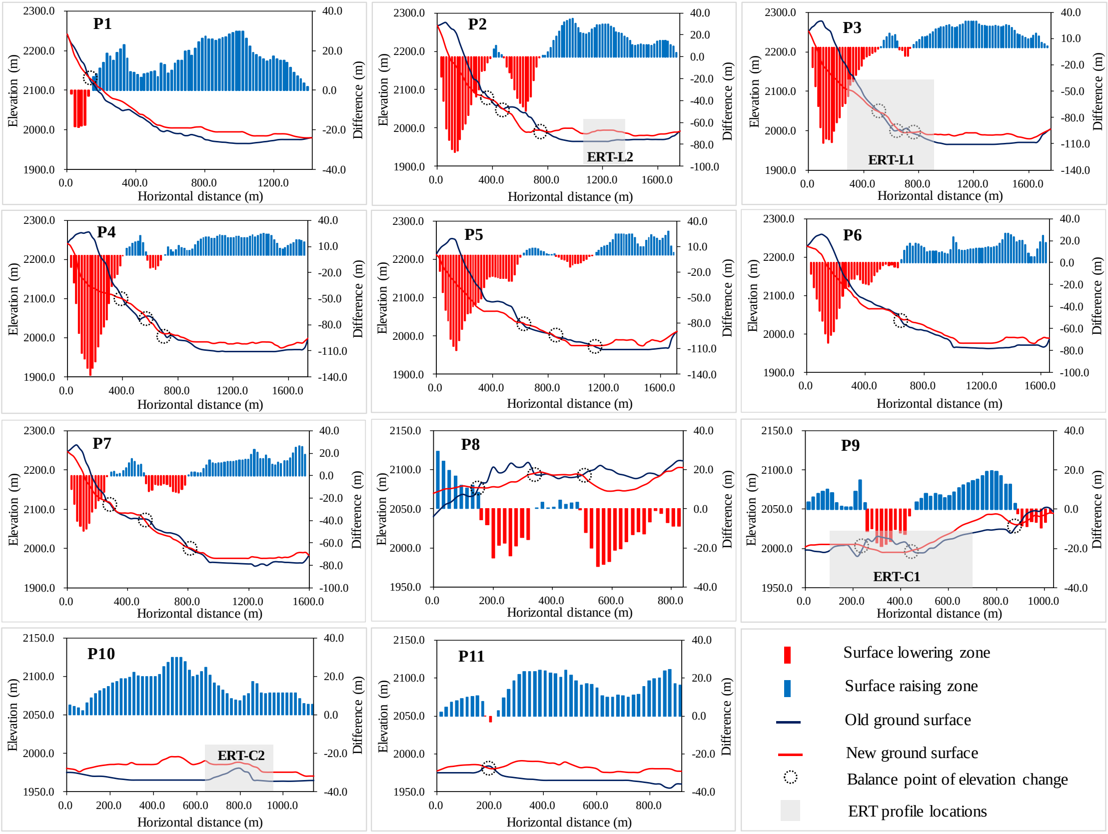
P1
P2
P3
P4
P5
P6
P7
P8
P9
P10
P11
ERT-L2
ERT-L1
ERT-C1
ERT-C2
Elevation (m)
Difference (m)
Horizontal distance (m)
Surface lowering zone
Surface raising zone
Old ground surface
New ground surface
Balance point of elevation change
ERT profile locations

Fig. 7

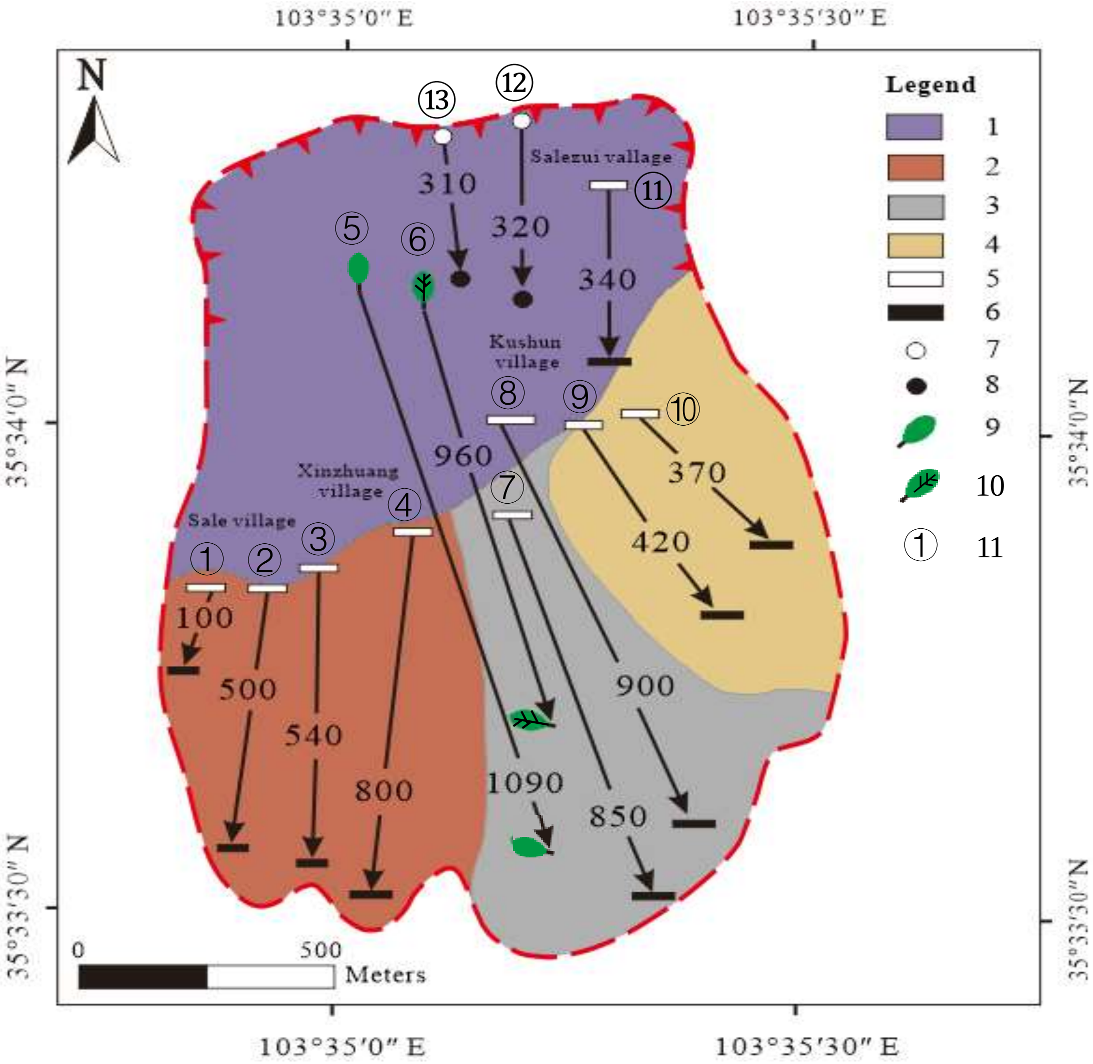
103°35′0″ E
103°35′30″ E
35°34′0″ N
35°33′30″ N
N
Legend
1
2
3
4
5
6
7
8
9
10
11
Salezui vallage
Kushun village
Xinzhuang village
Sale village
310
320
340
960
370
420
100
500
540
800
1090
850
900
0
500
Meters

Fig. 8

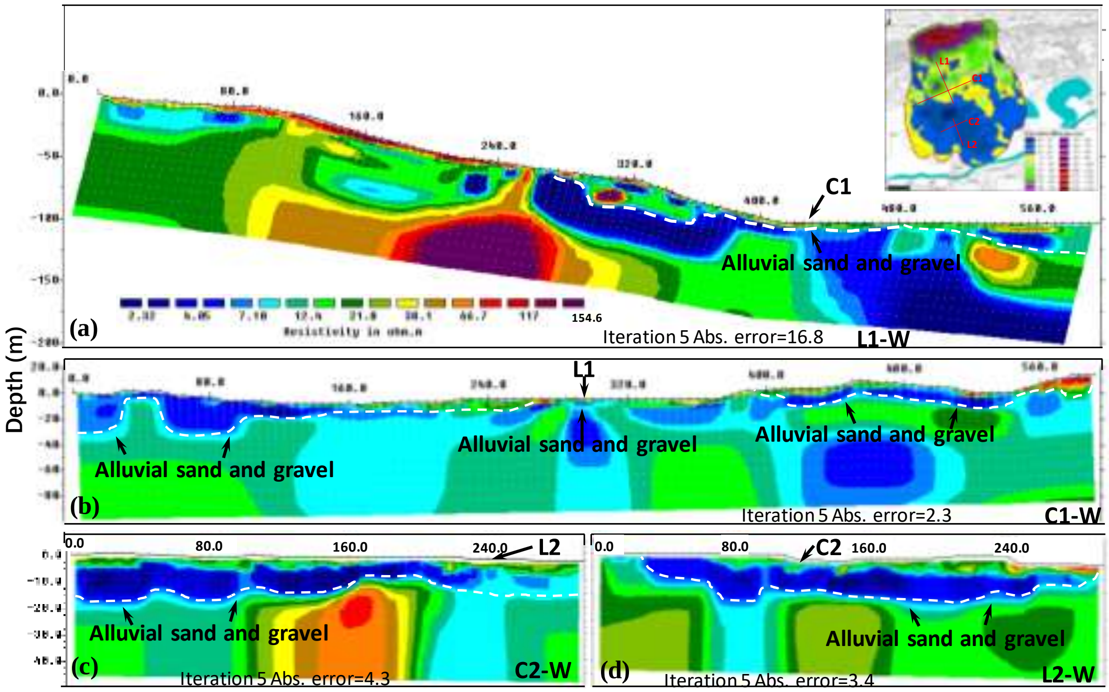

Depth (m)
C1
Alluvial sand and gravel
(a)
Resistivity in ohm.m
154.6
Iteration 5 Abs. error=16.8
L1-W
L1
Alluvial sand and gravel
Alluvial sand and gravel
Alluvial sand and gravel
(b)
Iteration 5 Abs. error=2.3
C1-W
0.0
80.0
160.0
240.0
L2
Alluvial sand and gravel
(c)
Iteration 5 Abs. error=4.3
C2-W
0.0
80.0
C2
160.0
240.0
Alluvial sand and gravel
(d)
Iteration 5 Abs. error=3.4
L2-W

Fig. 9

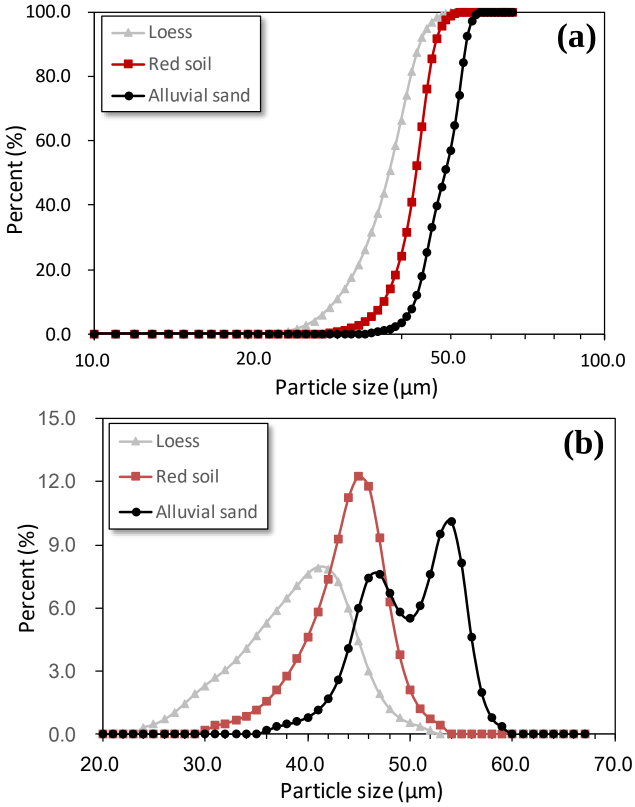
(a)
Loess
Red soil
Alluvial sand
Percent (%)
100.0
80.0
60.0
40.0
20.0
0.0
10.0
20.0
50.0
100.0
Particle size (μm)
(b)
Loess
Red soil
Alluvial sand
Percent (%)
15.0
12.0
9.0
6.0
3.0
0.0
20.0
30.0
40.0
50.0
60.0
70.0
Particle size (μm)

Fig. 10

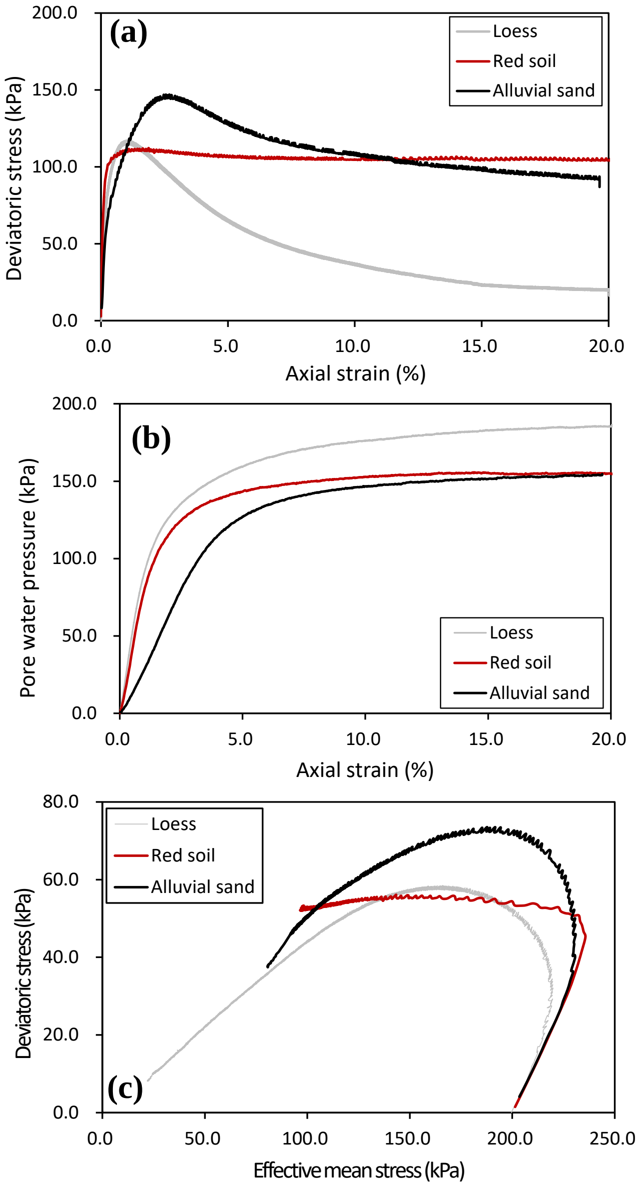
(a)
Deviatoric stress (kPa)
Axial strain (%)
Loess
Red soil
Alluvial sand
200.0
150.0
100.0
50.0
0.0
5.0
10.0
15.0
20.0
(b)
Pore water pressure (kPa)
Axial strain (%)
Loess
Red soil
Alluvial sand
(c)
Deviatoric stress (kPa)
Effective mean stress (kPa)
Loess
Red soil
Alluvial sand
80.0
60.0
40.0
20.0
0.0
50.0
100.0
150.0
200.0
250.0

Fig. 11

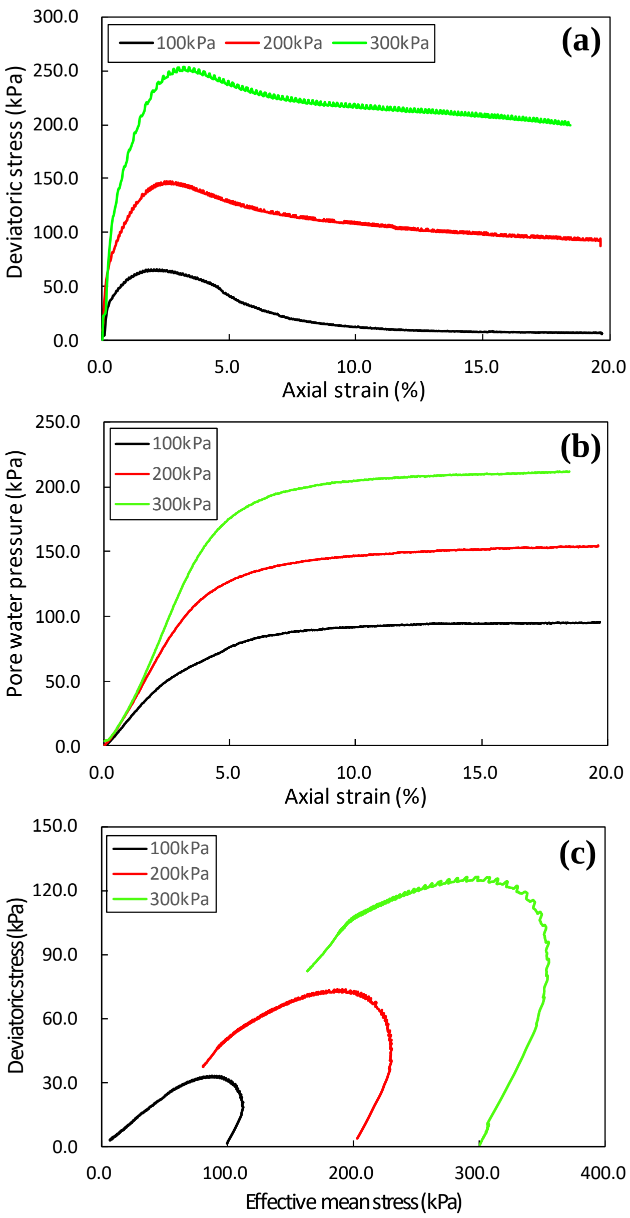
(a)
100kPa
200kPa
300kPa
Deviatoric stress (kPa)
300.0
250.0
200.0
150.0
100.0
50.0
0.0
0.0
5.0
10.0
15.0
20.0
Axial strain (%)
(b)
100kPa
200kPa
300kPa
Pore water pressure (kPa)
250.0
200.0
150.0
100.0
50.0
0.0
0.0
5.0
10.0
15.0
20.0
Axial strain (%)
(c)
100kPa
200kPa
300kPa
Deviatoric stress (kPa)
150.0
120.0
90.0
60.0
30.0
0.0
0.0
100.0
200.0
300.0
400.0
Effective mean stress (kPa)

Fig. 12

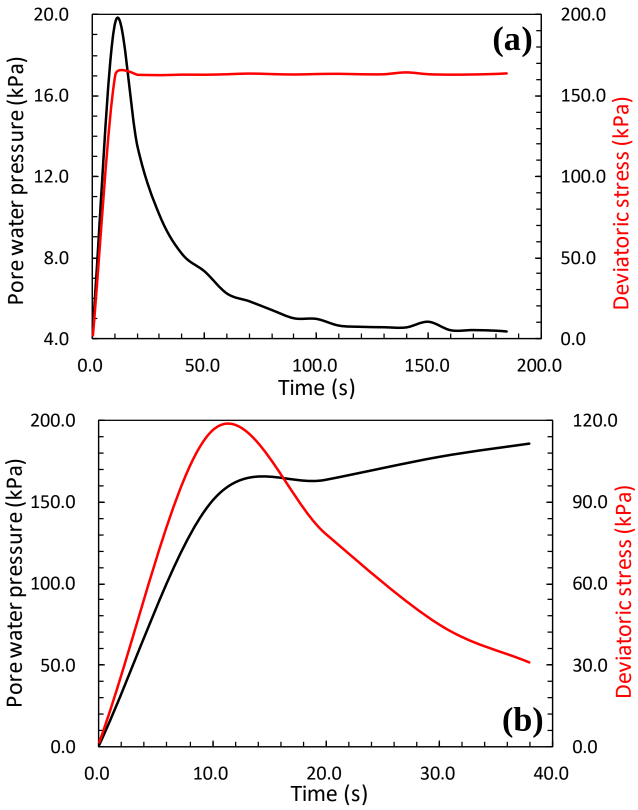

(a)
Pore water pressure (kPa)
Deviatoric stress (kPa)
Time (s)
20.0
16.0
12.0
8.0
4.0
200.0
150.0
100.0
50.0
0.0
0.0
50.0
100.0
150.0
200.0
(b)
Pore water pressure (kPa)
Deviatoric stress (kPa)
Time (s)
200.0
150.0
100.0
50.0
0.0
120.0
90.0
60.0
30.0
0.0
0.0
10.0
20.0
30.0
40.0

Fig. 13

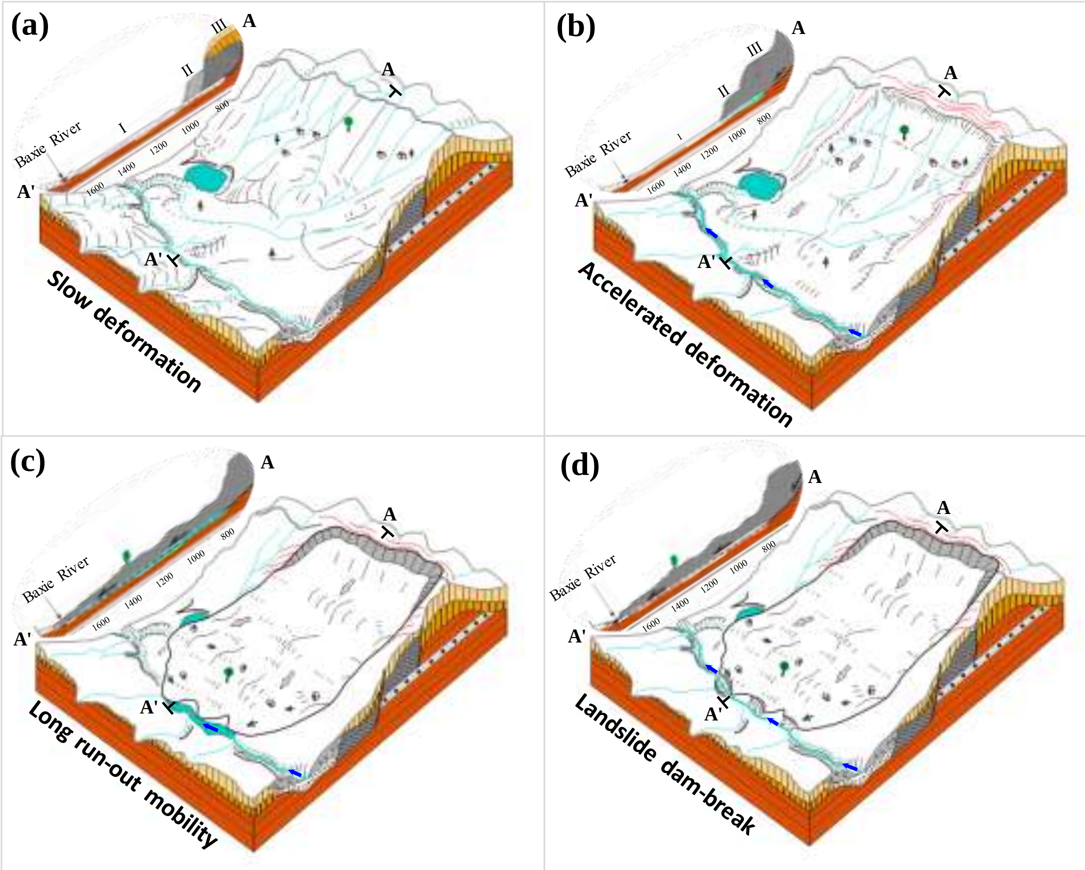

(a)
Slow deformation
(b)
Accelerated deformation
(c)
Long run-out mobility
(d)
Landslide dam-break
Baxie River
A
A'

Fig. 14

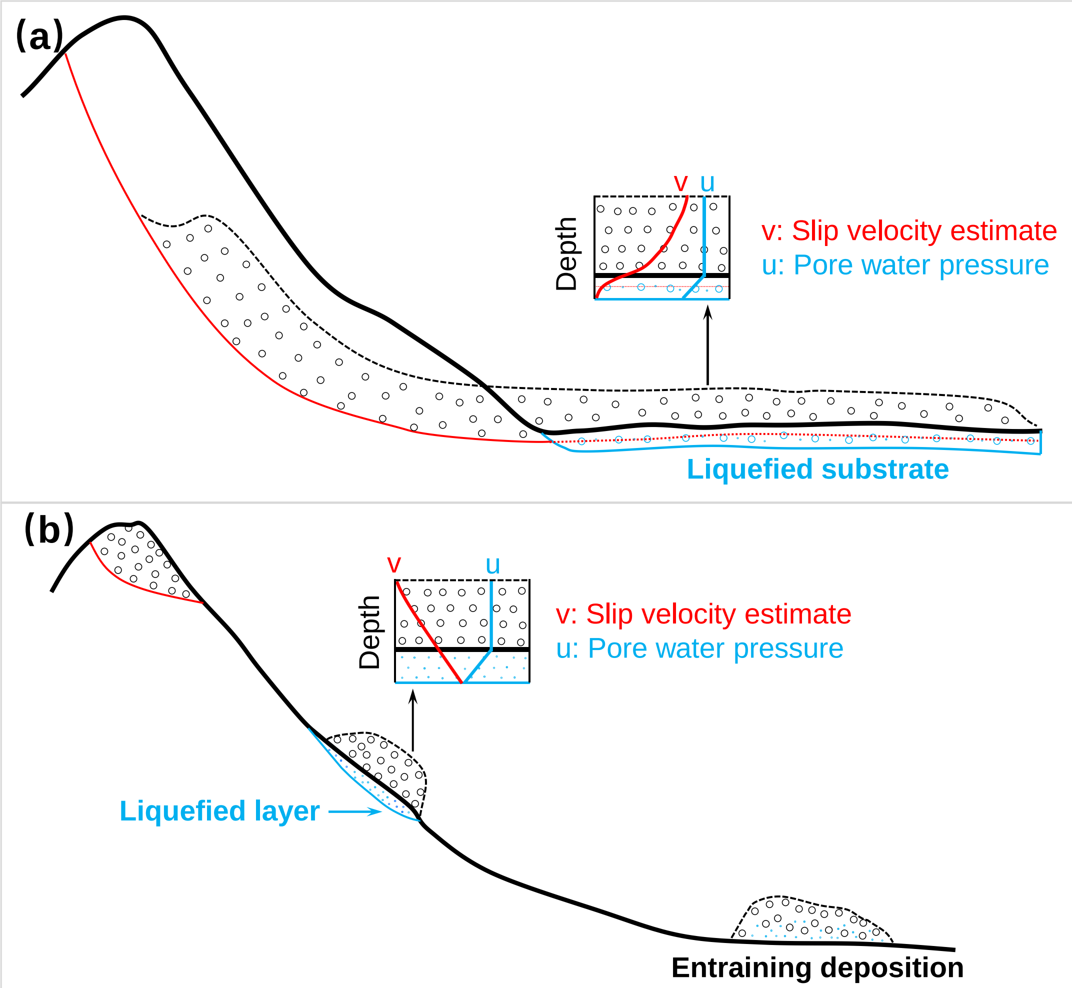
(a)
v
u
Depth
v: Slip velocity estimate
u: Pore water pressure
Liquefied substrate
(b)
v
u
Depth
v: Slip velocity estimate
u: Pore water pressure
Liquefied layer
Entraining deposition

Table 1: Kinematic parameters of different placemark locations on the Saleshan landslide

No.	PL	TD (°)	HD (m)	V (m/s)	AV (m/s)
1	WAZ	195	100	1.8	8.8
2		187	500	9.1	
3		183	540	9.8	
4		188	800	14.5	
5	CAZ	167	1090	19.8	16.7
6		173	960	17.5	
7		170	850	15.5	
8		166	900	16.4	
9	EAZ	150	420	7.6	7.2
10		149	370	6.7	
11	DZ	179	340	6.2	5.9
12		180	320	5.8	
13		175	310	5.6	

Note, No.: Placemark number; PL: Placemark location; TD: Travel direction; HD: Horizontal displacement; V: Velocity; AV: Average velocity; WAZ: West accumulation zone; CAZ: Central accumulation zone; EAZ: East accumulation zone; DZ: Depletion zone.

Title: A catastrophic flowslide overridden on liquefied substrate: The 1983 Saleshan landslide in China

Authors: Fanyu Zhang, Jianbing Peng, Xiugang Wu, Fazhen Pan, Yao Jiang, Chao Kang, Weijiang Wu, Wenguo Ma

Abstract: A flowslide overriding liquefied substrate can vastly enhance its disaster after failure initiation, due to rapid velocity and long-runout distance during landslides mobilized into flows. It is crucial to provide improved understanding to the mechanism of these catastrophic flowslides for hazard mitigation and risk assessment. This study focuses on the Saleshan landslide of Gansu in China, which is a typically catastrophic flowslide overrode a liquefied sand substrate. Geomorphologic and topographic maps along with analysis of seismic signals confirm its dynamic features and mobilized behaviors. ERT surveying detected abundant groundwater in the landslide, which is fundamental to its rapid long-runout distance. Particle size distributions and triaxial shear behaviors affirmed more readily liquefied behavior of superficial loess and underlying alluvial sand than red soil sandwiched them. We also examined the liquefaction susceptibility of the alluvial sand under loading impact at undrained and drained conditions. The alluvial sand is readily liquefied in the undrained condition while it is difficult at drained condition due to rapid water pore pressure dissipation. The results showed that the landslide experienced a sudden transformation from slide on the steep slope where it originated to flow on a nearly flat terrace with abundant groundwater that it overrode. This transformation can be attributed to the liquefied alluvial sand substrate enhancing the whole landslide body mobility. Along with recent, similar findings from landslides worldwide, substrate liquefaction may present a widespread, significant increase in landslide hazard and consequent mobility and our study reveals conditions necessary for this phenomenon to occur.

Keywords: Catastrophic flowslide, liquified substrate, mobilized transformation, Saleshan landslide, China

1. Introduction

Flowslide is generally catastrophic worldwide. This kind of flow-like landslides is always characterized by rapid velocity and long-runout distance during landslides mobilized into flows, as such they usually cause more catastrophic threats to people, environment, and property. Hence, it is curial to understand the mobility of these catastrophic flowslides to hazard mitigation and risk assessment.

Some studies have been conducted to gain understanding of rapid long-runout flowslides, involving field evidences, numerical and physical simulations, and shear tests, along with very few field monitoring (Hutchinson and Bhandari, 1971; Misfeldt *et al.*, 1991; Evans *et al.*, 2001; Wang *et al.*, 2003; Hungr and Evans, 2004; Crosta *et al.*, 2009a; Poschinger and Kippel, 2009; Iverson *et al.*, 2011; Crosta *et al.*, 2015; Iverson *et al.*, 2015; Collins and Reid, 2020). However, mechanisms resulting in flowslide mobility remain in debate, but some basic information is relatively clear. These studies showed that the catastrophic flowslides commonly occur a transformation from slide to flow. Furthermore, the transformed progress generally involves an undrained loading by overlying landslide mass, which is more prevalent in granular materials, such as sand, silt, and debris, along the flow path (Hutchinson and Bhandari, 1971; Wang *et al.*, 2003; Sassa and Wang, 2005). The liquefaction of the granular materials is crucial to maintain rapid and long-runout landside mobility (Hutchinson and Bhandari, 1971; Evans *et al.*, 2001; Take and Beddoe, 2014). Furthermore, the liquefied substrates have been considered vital to the transformed landslide mobility (Iverson *et al.*, 1997; Wang *et al.*, 2003; Iverson *et al.*, 2011). Nevertheless, Mangeney

(2011) argued that flow-like mobility could also occur in completely dry granular materials due to the lack of cohesion. Essentially, the mobility depends finally on the frictional or rheologic behaviors of sheared granular materials. Additionally, the transformation progress occurs in a channeling flow path, but also on a nearly flat surface. The former has been the focus of considerable research effort in recent years. In comparison, only few studies examined the transformation during movement from steep upper regions onto very flat slopes, focusing on the base liquefaction of the flat flow path (Hutchinson and Bhandari, 1971; Take and Beddoe, 2014; Crosta *et al.*, 2015). The 2014 Oso landslide obtained widespread attention to the catastrophic long-runout mobility on a nearly flat surface, due to the apparent presence of a liquified substrate (Iverson *et al.*, 2015; Iverson and George, 2016; Wartman *et al.*, 2016; Aaron *et al.*, 2017; Stark *et al.*, 2017; Collins and Reid, 2020). However, understanding the mobility of the flowslide on a nearly flat surface remains unclear, as evidenced by the broad range of hypotheses proposed to explain the well-studied Oso landslide's mobility.

Loess flowslides are among the most common of the flow-like landslides, as loess is prone to liquefaction under even an unsaturated condition. Earthquake and rainfall, along with irrigation, have become familiar triggers of the catastrophic loess flowslides in China. Earthquake-induced loess flowslides generally have long-runout mobility if shallow groundwater conditions are present, resulting in liquefied loess with high pore-water pressure and low shear resistance (Ishihara et *al.*, 1990; Wang *et al.*, 2014). Currently, rainfall and irrigation become more frequent triggers to the loess flowslides.

Many studies showed that infiltrated water elevates the groundwater, and cause the loess liquefaction forming the loess flowslides (Derbyshire *et al.*, 2000; Zhang *et al.*, 2014; Zhuang and Peng, 2014; Peng *et al.*, 2015; Peng *et al.*, 2017a; Peng *et al.*, 2017b; Zhang *et al.*, 2017; Zhang and Wang, 2018; Peng *et al.*, 2019). Visibly, water plays a dominant role in the occurrence of the loess flowslides. These studies mentioned above significantly improved our understanding of loess flowslides. Still, much of this effort has been in their initiation and failure mechanisms, examining the liquefied behavior of the loess. Some studies of the mobility of the loess flowslides focused on numerical simulation and field evidence (Peng *et al.*, 2015; Zhang *et al.*, 2017; Kang *et al.*, 2018; Li *et al.*, 2019). Yet there still remains an urgent problem to understand the mobilized mechanisms of a landslide from a slide on the steep upper slope that transforms into a flow on a nearly flat terrace. Such slides frequently threatened the residents and their properties, and also cause major ecological and environmental problems.

This study aims to provide an improved understanding of the transformed mechanism from slide to flow overridden on a liquified substrate. We study a catastrophic flowlside, i.e., the Saleshan landslide of Gansu in China, which killed . We produced geomorphologic and topographic maps for analyzing the movement features of the landslide using cartographic and GIS techniques. We performed electrical resistivity tomography (ERT) to detect groundwater conditions on the landslide body and the terrace. Furthermore, we examined the particle size distributions and triaxial shear behaviors of loess, red soil, and alluvial sand from the landslide deposited zones. We especially performed two loading impact tests on the alluvial sand specimens under drained and undrained status. Finally, we discussed the transformed mechanism of this kind of landslide from slide on steep slopes to flow on gentle terraces, and compare the difference in the liquified entrainment occurred in a steep channel bed erosion along its flow path. Our findings afford some fundamental knowledge to the mobility of this kind of flowslides overridden on a liquefied substrate, and specific assistances for landslide hazard mitigation and risk assessment.

2. Saleshan landslide background

The Saleshan landslide is situated in Dongxiang County, Gansu Province, China (Fig. 1a), and occurred on an afternoon at about 5:46 local time on 7 March 1983, which caused 237 deaths and damage of the four villages. Hence, the Saleshan landslide is among the most disastrous one in the Baxie River catchment, which has hundreds of different types of loess landslides at various sizes (Fig. 1b). Following the updated Varnes landslide classification system, Hungr *et al.* (2014) described the Saleshan landslide as a flowslide, which is characterized by long runout distance traveled across a nearly flat surface. Fig. 1 c and d present the panoramic views of the Saleshan landslide in 1983 and 2015.

2.1 Geological structures

Fig. 2 shows the simplified stratigraphic and topographic section through the pre-landslide topography and the Saleshan landslide along its main sliding direction. The presented stratigraphic and topographic section is revised to the previous version from Zhang and Wang (1984) and Zhang *et al.* (2002). The geological structures can be referred to in the previous studies (Zhang and Wang, 1984; Zhang *et al.*, 2002).

To geological structures before failure (Fig. 2a), the stratigraphic section of the Saleshan landslide include in descending order: (1) Late Pleistocene Lishi Loess (Q_2), (2) Middle Pleistocene Malan Loess (Q_3), (3) Pliocene mudstone and Cobblestone (N_2), (4) Quaternary alluvial sand and gravel, colluvial mudstone and loess (Q_4). The alluvial sand and gravel is located on the first terrace. Moreover, the previous studies speculated that the colluvial mudstone and loess is the deposition of a historical landslide situated over the first terrace (Kang *et al.*, 2018). There are no folds and faults in Saleshan landslide area, which exhibits a simple geologic structure (Zhang *et al.*, 2002). Nevertheless, there are two sets of dominant joints, in which the east-west set is matched with cracks in the main scarp of Saleshan landslide (Zhang *et al.*, 2002).

To geological structures after failure (Fig. 2b), a simplified stratigraphic section can be described as follow: (1) the displaced material of landslide body covered over the alluvial sand and gravel on the first terrace; and (2) the alluvial layer overlies the undisturbed mudstone bedrock. Zhang *et al.* (2002) considered that the alluvial sand and gravel is undisturbed on the first terrace, while other authors argued that the landslide ploughed or impacted the alluvial layer, leading to erosional liquefaction of the substrate (Wang *et al.*, 1988; Kang *et al.*, 2018). It is interesting to note the life-saving tree on the landslide. When the Saleshan landslide occurred, a person tightly held the tree, moving about 960 m without any injures (Zhang *et al.*, 2002; Kang *et al.*, 2018).

2.1 Geomorphologic characteristics

The Saleshan landslide is located on the south facing side of a steep slope ridge on the northern side of Baxie River. The geomorphologic characteristic change of the Saleshan landslide mainly depends on the Baxie River terraces (Fig. 2). The elevation of the Saleshan landslide ranges from 1950 m to 2280 m, including four terraces with abrupt slope angle change. The top of the slope ridge is 2280 m elevation above the fourth terrace, where the slope angle is larger than 50°. The fourth terrace is located between 2195 m and 2080 m elevation, with a slope angle varying from 30° to 35°. The third and second terraces have developed two gentle platforms, and their elevation varies from 2080 m to 1970 m with a switched deep slope with an average 30° slope angle. The lowest first terrace is about 800 m away from the toe of the Saleshan slope with nearly flat surface topography before slope failure. After the Saleshan slope failure, the first terrace became the main accumulation zone. The topographic change reveals that the Saleshan landslide failed from a deep upslope and moved on a flat surface with easy liquified sand and gravel layer, which means an abrupt transformation of movement style. This also indicates that the geologic structure and geomorphologic characteristics is basic conditions for the long-runout mobility during Saleshan landslide propagation.

2.3 Hydroclimatic conditions

The Baxie River basin is a semiarid climate environment. Commonly, the average annual precipitation is 485 mm, with 80% of the total in the period from June to September, and frequent rainstorms in summer (Zhang *et al.*, 2002; Kang *et al.*, 2018). However, the climate presents a wetter environment since 1979, with annual precipitation of 650 mm, and the winter precipitation in 1982 was also above average reaching 66.3 mm (Zhang *et al.*, 2002). There has meltwater before failure in March 1983. Thus, the freeze-thaw effect was suggested to trigger the Saleshan landslide (Huang, 2009). However, Kang *et al.* (2018) considered that the meltwater effectively elevated groundwater, which would be attributed to progressive failure.

The groundwater is of phreatic water, which has all distributed below the fourth terrace (Ma and Qian, 1998). Many springs overflow from the toe of the terraces on both sides of the River valley. Notably, the shallow aquifer on the first terrace is known from borehole information, and the depth of the groundwater table is about 2 m below the ground surface (Ma and Qian, 1998). Besides, the storage water in the Jiuer reservoir was used to the agricultural irrigation on the terraces, guaranteeing the long-term shallow groundwater level. The groundwater information provides useful help to understand the mobility of the Saleshan landslide.

Notably, no observed earthquake and rainfall was recorded in the Baxie River basin in March 1983. Therefore long-term accumulated precipitation and irrigation, rather than abrupt seismic shaking and rainfall infiltration, likely played a key role in initiating the Saleshan landslide.

3. Materials and methods

3.1 Geomorphological features mapping

The geomorphological mapping provides geomorphologic characteristics as an important aid for understanding the inherent problems on the propagation of the landslide. For this purpose, we collected various data from old photos, field investigations, remote images, previous references about Selanshan landslide, and produced a graphical map of geomorphologic imprints using cartographic and GIS techniques. The geomorphological map in this study is representative of many results both from various published data and unpublished reports.

3.2 Topographic changes detection

The topographic change detection is a fundamental prerequisite for landslide deposition thickness but also can provide a direct result assessment for landslide numerical modeling. In this context, we first prepared two large scale topographic maps at the scale of 1:10000 from before and after slope failure, and digitized the two maps using ArcGIS software, and then constructed their digital elevation models (DEMs). After which, we compared and analyzed the topographic change using the Geomorphic Change Detection (GCD) 7.0 software (http://gcd.riverscapes.xyz/), which is a powerful tool on geomorphological change detection (Wheaton *et al.*, 2010; Wheaton *et al.*, 2015). The GCD produced DEM of Difference (DoD) maps before and after the Saleshan landslide, and estimated the net change in geomorphologic features, such as elevation, volume, area.

3.3 Movement features analysis

To analyze mobility after slope failure, we produce a map of movement features, including motion displacement, motion direction, and motion velocity. The motion displacement derives a direct estimate from the placemarks on landslide body, including the sites from house and tree before and after failure. We also record the motion direction of all the placemarks referred to the previous research results (Wang *et al.*, 1988). We also calculated the motion velocity from displacement over time at different sites of the Saleshan landslide. The mobility time derives from seismic signals induced by Saleshan landslide at three seismic stations. The detailed procedure can refer to the supplementary, involving how to digitize old analog seismograms to obtain the relatively accurate time using a MATLAB™ toolbox of DigitSeis developed by Bogiatzis (2015), with slight help of manual processing, to revitalize only three NS analog seismograms from the three seismic stations (Supplementary note, Figs. 1 and 2).

3.4 Textural and mechanical properties test

To obtain the textural and mechanical properties, we taken disturbed loess and red soil (product of mudstone) specimens close to the scarp of the Saleshan landslide, as well as an alluvial sand specimen on the first terrace of Baxie River. These specimens were oven-dried and disaggregated using a rubber hammer. We analyzed particle size distributions of all the samples using a Microtrac S3500 laser diffraction instrument.

Each specimen tested eight times for consistency.

We conducted a series of consolidated undrained compression (CUC) triaxial tests on all the three samples, and two quasi-dynamic impact stress loading (QSL) drained and undrained triaxial tests on the alluvial sand samples. All the specimens have a height of 10 cm and a diameter of 5 cm. All the examples were saturated by carbon dioxide replacement, de-aired water flushing, and back pressure saturation. The specimens were consolidated under a specified cell pressure and then compressed under undrained conditions by means of the strain-controlled method. The axial strain was increased at a rate of 0.01% per minute. The specimens were consolidated and tested at cell pressures of 100, 200, 300 kPa. In CUC sets, compression at each cell pressure was terminated when the axial strain close to 20%. In QSL sets, the specimens were compressed by utilizing a sinusoidal stress loading module, but in which we used a quarter loading period to load 160 kPa with 10 seconds at cell pressures of 200 kPa. Notably, if the stress loading velocity is too rapid, this maybe generates a damage to the triaxial apparatus. We performed one drained stress loading test, and other for the undrained condition.

3.5 Electrical resistivity survey

To prospect the internal structure and hydrological environment of the Saleshan landslide, we carried out four electrical resistivity tomography (ERT) profiles (see their locations in Fig. 5) to obtain a detailed characterization about the electrical signals in the first tens of meters below the ground surface. During the field survey, we used a multielectrode system with 120 electrodes both in Wenner-Schlumberger and Wenner arrays with an electrode spacing of 5 m. We located these electrical profiles using a GPS and measured their topographic changes using a laser measuring technique. Finally, we inverted the apparent resistivity data by a tomographic inversion technique using the newest RES2DINV software. During the inversion, we implemented a smoothness-type regularization constrained least squares by using incomplete Gauss-Newton optimization technique, taking the topographical changes into account along the profiles. The optimization technique is to iteratively adjust the resistivity to obtain a minimal difference between the calculated and measured apparent resistivity values. The absolute acceptable error provides a measurement of this difference.

4. Results

4.1 Geomorphologic imprints

The geomorphologic imprints on a landslide provide direct observation and object analysis for dynamic features at different zones, but is important base to hazard management land planning after the landslide. Fig. 3 shows the geomorphological map of Saleshan landslide, which is a revised version based on the previous conclusions (Zhang *et al.*, 2002; Wu and Wang, 2006). Our geomorphological map presents an immediate and complete description of remaining features at different locations throughout the landslide. From the viewpoint of space elements, we divide the geomorphologic features into three styles. The dotted imprints only have spring outcrop places. The linear features include zone boundaries, major and minor scarps, various cracks, groundwater drainage, and surface water recharge. The planar features involve depressions and hillocks in the zone of depletion, and grooves and hummocks in the zone of accumulation, along with river gully and reservoir adjacent landslide.

There are several critical features worth analyzing. First, the different types of cracks portray the deformation behaviors at respective locations. The cracks distributed on the crown portray tensile deformation, and the lateral and transverse cracks that occurred on the flank signify tractive deformation and fracturing process. These radial cracks emerge thrust behavior on the toe. The depressions and hillocks underwent extension and compression during the landslide movement. The significant number of hummocks on the zone of accumulation show the evidence of fluidization and extension during landslide mobility. There are more in the west-slide and central regions than in the east slide in the zone of accumulation. Using hummocks that explain the motion behavior of the fluidized landslides has also been paid special attention by other authors (Paguican *et al.*, 2014; Collins and Reid, 2020; Dufresne and Geertsema, 2020). The hummocks on a landslide can reveal important movement features during their motion.

Fig. 4 shows the old photographs illustrating typical geomorphological imprints of the Saleshan landslide. These photographs were taken shortly after the landslide in 1983. They not only well verify the evidence from the geomorphological map (Fig. 3), but some of them provide more intuitive clues to uncover movement behavior. As shown in Figs. 4c and 4d, the standing cow and life-saving tree reveal that the displaced materials were incompletely disturbed, mainly maintaining the original stratigraphic structure. Thus, we can speculate that the landslide body moved along a slip surface with low shear resistance. Also, we observe differential movement on the zone of accumulation, due to differences in disturbance and liquefaction of the displaced materials (Fig. 4i-Fig. 4l). The loess at right flank is completely liquified (Fig. 4i), and the deposit at the toe dammed the Baxie River gully with high water content (Fig. 4j). While the deposit close to left flank buried the Jiuer reservoir (Fig. 4k), but they hold some original structures presenting a low water content context.

From the geomorphologic imprints and evidence, we suggest that the Saleshan landslide exists a motion transformation from slide to flow and that the flow-like materials failed along a week slip surface with some differences in deposit features. Meanwhile, this evidence affords clues to analyze the characteristics of accumulation and mobility after slope failure.

4.2 Topographic changes

There are few accurate measurements of the volume of a historical landslide, because of a difficulty gaining the pre- and post-landslide topographic data. Fig. 5a shows the elevation difference of the pre- and post-landslide on the Saleshan landslide. Fig 5b and 5c show geomorphic change detection, the areal and volumetric elevation change distributions. The negative elevation is for erosion, and positive elevation is for accumulation, respectively. The elevation change range of erosion area is −142 to 0 m, which located on the depletion zone. The elevation change range of accumulation distributes between 0 and 39 m occurred in the accumulation zone. Volume proportions of erosion and accumulation are almost the same, which are 55.69 and 44.31%, respectively. The decrease of accumulation volume may be due to the part of loess flowing into Baxie river and Jieer reservoir. The areal proportion of erosion (35.11%) is about half as much as deposition (64.89%).

To better detect the dynamic process of landslides, such as the change of area, volume, and elevation in pre- and post-landslide, we used the Geomorphic Change Detection (GCD) 7.0 software to construct seven two-dimensional profiles of the slip surface in the movement direction and four profiles perpendicular to the movement direction (Fig. 5a). By analyzing the profiles (Fig. 6), we can further understand the characteristics of the topographic change of the Saleshan landslide. With steeper slopes, the erosion probability is higher, and the maximum erosion height up to 139 meters, while the majority of accumulation occurs on the flat areas (P1-P7). It also can be found that erosion mainly occurs on the fourth terrace, and the first terrace is the accumulation zone. The accumulation and erosion features are related to the evidence from geomorphologic characteristics. For the four profiles perpendicular to the movement direction, the degree of erosion at area of P8 and P9 is much greater than that of P10 and P11. As P8 and P9 is located at the trailing edge of the landslide, others are at the leading edge of the landslide. Likewise, hillocks and scarps at the trailing edge of the landslides are eroded, while gullies are piled up and filled. These profiles describe the exterior morphological features and structures in the horizontal and vertical directions, and it can highlight some changes in pre- and post-landslide.

4.3 Rapid and long-runout mobility

In the mobility of the rapid and long-runout landslides, its velocity, displacement, and direction are vital kinematic parameters. Nevertheless, they are often uncertain because this is practically difficult to identify the kinematic parameters accurately. However, the surviving placemarks, e.g., tree and house, could be useful in the dynamic analysis. Fig. 7 shows the motion displacement vector at different placemark locations on the Saleshan landslide, and the calculated kinematic parameters are listed in Table 1. Among these placemarks, there is the most significant motion displacement of 1090 m and the highest motions velocity of 19.8 m/s. The results reveal that the Saleshan landslide underwent rapid and long-runout mobility, in which appeared apparent variable zonation of motion.

On the depletion zone, the three placemarks are almost the same with the horizontal displacements from 310 to 340 m, which means that the vertical fall is significant in the zone (see Fig. 1b). There has the lowest average velocity of 5.9 m/s in the whole landslide zones with a velocity between 5.8 and 6.2 m/s. Due to the calculated velocities on the total mobilized time of 55 seconds, the velocity of the depletion zone may severely be underestimated in the three placemarks. The previous dynamic studies and eyewitness account showed that the velocity of the sliding blocks both exceeds 20 m/s in the depletion zone (Miao *et al.*, 2001; Zhang *et al.*, 2002; Kang *et al.*, 2018).

On the accumulation zone, the displacement vectors present distinct kinematic differences. The placemarks of the central accumulation zone have the greatest motion displacement with the highest landslide velocities. There have relatively more significant displacement and velocity on the west accumulation zone than on the east accumulation zone. It should be noted that there have relatively low velocity and small motion displacement closer to both the flanks. It is consistent with the field evidence (Fig. 4k). This means that the displaced materials immediately stop after rupturing the slide surface. In addition, the motion directions of the various placemarks depend on the original topographic changes and geomorphologic features (Fig. 3 and Fig. 4).

In sum, the Saleshan landslide was rapid in the progress of long-distance motion. The motion of Saleshan landslide primarily occurred on the accumulation zone, in which the velocity and displacement of the displaced materials decrease from the central zone to two flanks. The motion features are matched with the evidence from geomorphologic maps and topographic changes (Fig. 3~Fig. 6). Besides, the underestimated velocity derived from displacement and time may result in some misleading to kinematic analysis.

4.4 Structural and hydrological constraints

ERT is widely used in landslide investigation characterized by a complex geological setting (Perrone *et al.*, 2014). And recently time-lapse ERT is increasingly applied in long-term landslide monitoring (Grandjean *et al.*, 2011; Chambers *et al.*, 2013; Wilkinson *et al.*, 2016; Crawford *et al.*, 2019). Thus, ERT used as a conventional geophysical prospecting method to the geological structure and hydrological environment of a landslide, now becomes a convenient technology using in-situ landslide monitoring.

Fig. 8 shows the interpreted Wenner ERT sections of four profiles on the Saleshan landslide, and the detailed location of the four profiles are shown in the index figure and Fig. 6. The profile L1 is longitudinal through the front zone of depletion, and the end zone of accumulation along movement direction (Fig. 8a), and the profile C1 is transverse through the toe region of rupture surface (Fig. 8b). In addition, the interpreted Wenner Schlumberger ERT sections of four profiles are shown in Supplementary Figs 3. The profiles L1 and C2 profiles orthogonally cross through the middle zone of accumulation on the first terrace (Fig. 8c and d). In the profile L1, the high resistivity sections correspond with the front zone of depletion with relatively low water content and complete structure, while the end zone of accumulation presents low resistivity. The information disclosed from ERT image is matched with the data of borehole after the landslide (Wu and Wang, 2006), along with in-situ investigation. Notably, there is an abundant phreatic region around the rupture surface. It can be verified the evidence from the spring exposed on the third and fourth terrace, along with the surface water convergence in the gully (See Fig. 3). The low resistivity in the profile C1 is consistent with the gully sites, where there has high water content in lowland causing thinker deposit and greater mobility (See Fig. 6). Meanwhile, the toe zone of the rupture surface has relatively lower resistivity, comparing with the zone of depletion. The information from profiles L1 and C2 shows that the displaced materials thickness vary between 15 and 20 m, and that they deposited on the original ground surface (Fig. 6). The deposit is thinner closer to the tip of the Saleshan landslide.

Notably, the sediments below the farmland ground exert a very low resistivity signifying a high water content condition. This is well-matched with direct field observations after the landslide, such as loess liquefaction and deposit with high water content (see Fig 4j and Fig 4l) on the west zone of accumulation.

The electrical resistivity could obtain useful geophysical signals varying with the nature and state of granular materials, as well as the fluid in the granular medium. Thus, the four ERT survey images add information on the internal structure of the Saleshan landslide, which is consistent with the geomorphologic features and topographic changes. Meanwhile, the ERT images well provide the hydrological information, which helps the understanding of the propagation of the Saleshan landslide.

4.5 Liquefaction behaviors

4.5.1 Particle size distribution

The particle size distributions are often crucial for appraising liquefaction potential of flow slides (Kramer, 1988; Picarelli, 2010), and could be indirectly used to interpret liquefaction behaviors of fine granular soils. Fig. 9 shows the exemplified particle size distribution of the three types of soil on the Saleshan landslides. To facilitate a much clearer view of particle size, Fig. 9b uses a linear abscissa, rather than a logarithmic abscissa. Other repeated test results were shown in Supplementary Figs. 4. The three samples are silty soils with uniform gradation. The loess has the greatest fine fractions, and the alluvial sands include the coarsest fractions, whereas the red soil is intermediate. Note that there are two modes on the frequency curves with two unimodal curves and one bimodal curve. The loess and red soil have both a smooth unimodal frequency distribution curve. The loess has a single fine component with a size boundary of 20-60 µm and mean practice size (D_{50}) of 38 µm. The texture of the red soil is like that of the loess, but it has a deviation with a size range of 25-55 µm, and a mean practice size of 43 µm. This kind of deviation may derive from the modification of weathering processes of mudstone. The alluvial sand has a bimodal frequency distribution of particle size, and the range is from 25 µm to 60 µm with a mean practice size of 48 µm. Generally, the bimodal sand is a typical production of a modern alluvial or fluvial environment (Taira and Scholle, 1979; Sun *et al.*, 2002). Compared to evidence from the particle size distribution in other flowslides (Kramer, 1988; Picarelli, 2010; Zhang *et al.*, 2019), all the three samples on the Saleshan landslide are characteristic of liquefaction features, which have the potential to liquefy when close to saturation.

4.5.2 Shear properties

It is still necessary to examine the shear properties of soil to understand its liquefaction behaviors directly. Fig. 10 compares the results of the undrained triaxial shear tests of the three soils on the Saleshan landslide at the same confining pressure (i.e., 200 kPa). Fig. 10a and b present the change deviator stress and pore water pressure with axial strain. Fig. 10c depicts an effective stress path. The three specimens have apparent differences in liquefication behaviors. The loess specimen shows a typical strain behavior maintaining high pore water pressure with an obvious decrease in strength after peak value. The results are consistent with those observed in the liquified or collapsed loess elsewhere (Zhang *et al.*, 2013; Wang *et al.*, 2014; Zhang *et al.*, 2014; Zhang and Wang, 2018). This means that the loess in Saleshan landslide area has visible liquefaction behavior under undrained condition, which is matched with in-situ evidence (Fig. 4i). Notably, the red soil has the lowest liquefaction potential with very light strength decrease after peak strength, although its particle size distribution is located between loess and alluvial sand. It may be related to the strong cementation or bonding existing in the weathering products of mudstone, which could attribute to more clay fractions in the red soil. The alluvial sand specimen has the most significant increase in pore water pressure after the peak strength. As shown in Fig. 9, the alluvial sand is comprised of fine sand, and finer suspended muddy. The small amount of suspended muddy slightly decreases the liquefication of the alluvial sand. Similar results have been found in ring shear and triaxial shear tests (Wang *et al.*, 2007; Carraro *et al.*, 2009).

Fig. 11 shows the undrained triaxial test results for the alluvial sand specimens. The deviator stress of all the specimens increases a peak value with increasing axial strain; after that, abruptly decreases a steady-state with further increase in axial strain (Fig. 11a). Meanwhile, the pore water pressure continuously increases to a steady value with increasing axial strain (Fig. 11b). The effective stress paths show that pure contractive behavior during undrained compression shearing (Fig. 11c). These results further support that all the alluvial sand specimens present unusual liquefaction behavior, and that is more prominent at low confining pressure.

Fig. 12 shows the triaxial test results from quasi-dynamic impact stress loading of the alluvial sand specimens under drained and undrained conditions. In the drained condition, the pore water pressure increases rapidly to 20 kPa in the progress of the impact loading (i.e., 10s), and after that, it has an obvious decrease with almost constant loading deviatoric stress of 160 kPa (Fig. 12a). Meanwhile, the generated pore water pressure dissipated gradually with 100 s. The relatively high dissipation rate in pore water pressure could be attributed to its inherent granular characteristics (Fig.9). This is in contrast to the behavior exhibited in undrained impact loading, and the pore water pressure is the same rapid increase as the drained impact stress loading (Fig. 12b). The desired impact stress could not fully load on the samples, and it has completely collapsed with a rapid increase in pore water pressure. After that, the pore water pressure slightly increases and, accordingly, a striking decrease in deviatoric stress. It is essential for a structural collapse with a great axial displacement. The results show that impact can generate pore water pressure on the alluvial sand, and the undrained impact loading is easier to produce pore water pressure on the alluvial sand than under drained conditions. Meanwhile, the quickly dissipated pore water pressure on the alluvial sand may contribute to the liquefaction of the loess, and consequently enhanced the mobility of the Saleshan landslide. This finding is consistent with those research results from ring shear tests (Wang *et al.*, 2003) and numerical simulation (Collins and Reid, 2020).

4. Discussion

4.1 Transformation from a slide on the steep slope to flow on the gentle terrace

The Saleshan landslide experienced a typical transformation from progressive slide to catastrophic flow, i.e., velocity transition from slow to fast. The progressive deformation along a sliding surface went through more than four years from the evidence of monitoring data and eyewitness account, while the disastrous mobility after failure initiation only underwent 60 seconds with about 1000 m mobility (Wang *et al.*, 1988; Miao *et al.*, 2001; Zhang *et al.*, 2002; Wu and Wang, 2006; Kang *et al.*, 2018). Fig. 13 shows the hypothesized sequence from progressive deformation to the catastrophic mobility of 1983 Saleshan landslide. The stage from slow to accelerated deformation resulted in the pore water pressure accumulation in the toe zone of the slope (Fig. 13a and b). After that, the landslides on dissected steep mudstone slope transformed into a flow-type landslide that travels long runout distance across a nearly flat terrace (Fig. 13c). Finally, the elevated reservoir water triggered landslide dam-break (Fig. 13d). The previous studies have well analyzed the deformation mechanism of the Saleshan landslide, but the unexpected flow-type mobility remains unclear. Thus, we focus here on the transformation mechanisms from the slide on steep upper slope to flow on nearly flat terrace.

The transformed landslide from slide to flow could be attributed to the unusual structural and hydrological configurations of the toe and travel zone of the Saleshan landslide. There is enough surface and sub-surface water convergence, leading to a shallow groundwater level in alluvial sand layers with high liquefaction potential on the first terrace. The evidence can prove the speculation from geomorphologic mapping (Figs 2 and 3), ERT survey (Fig 8), and test results (Figs. 9-11). Generally, the groundwater condition is key to the transformation from progressive slide to catastrophic flow in the Saleshan landslide; meanwhile, the highly susceptible to liquefaction alluvial sand is essential to the transformation. On the whole, the transformation strictly depends on the liquefied substrate, i.e., alluvial saturated or even partly saturated sand layer on the first terrace. Of course, as revealed by results in field and laboratory (Figs. 3-5 and Fig. 10), the highly liquefied loess has a particular contribution to the mobility after failure.

In the Chinese Loess Plateau, identical loess flowslides have frequently occurred on the Jingyang platform (Xu *et al.*, 2009; Peng *et al.*, 2017a; Peng *et al.*, 2018; Li *et al.*, 2019). These researchers also proved that the hydrogeological conditions on the nearly flat river terrace close to the current Wei River, i.e., the alluvial sand layer and high groundwater level, control the transformed progress. Incorporating with evidences from liquefied sand pipes observed in loess deposits (Xu *et al.*, 2009) deduced a conceptualized liquefaction model in double layers (i.e., sand and loess) along sliding surface on the nearly flat terrace. Peng *et al.* (2018) excavated several big exploratory trenches on the accumulation of the flowslides, and they found typical liquefied evidence of sand pipes and sand boils intruded into loess deposits. However, it lacks direct ground evidence, which can be attributed to the thick loess deposits with relatively low permeability. Also, the numerical simulation and shear wave detection supported that liquefaction entrainment of the terrace sand deposits controls their rapid and long runout mobility of those loess flowslides (Peng *et al.*, 2017a; Li *et al.*, 2019).

In the rest of the world, there have been similar structural and hydrologic constraints with the above loess flowslides, which resulted in the same transformation from slides on steep upper slope to flows with high mobility on a gentle lower terrace. A famous example in Switzerland is the Flims rockslide avalanche, which liquefied alluvial deposits on the terrace, leading to about 13 km displacement and damming of the Vorderrhein river valley (Poschinger and Kippel, 2009). There was observed the sub-vertical tubes of gravel composition almost without any fines in the landslide deposits (Pavoni, 1968), and these finer materials such as sand and silt have been washed out during water flow (Pavoni, 1968; Poschinger and Kippel, 2009). This is a typical feature of liquefaction of alluvial deposits. The scholars in Czech Republic found that a massive rockslide avalanche transformed as a long-runout landslide along the terrace in the Bilina river (Burda *et al.*, 2018). The data shows that the slope of the terrace is generally lower than 10 degrees in this study region (Poschinger and Kippel, 2009; Burda *et al.*, 2018). In Saskatchewa river, there have many landslides dissected on shale slopes; some of them transformed into a fluidized landslide that mobilized far beyond that expected on a nearly flat terrace. Moreover, multiples boreholes revealed that the sliding surface is located on Tertiary sand in the Hepburn aquifer system (Misfeldt *et al.*, 1991). Thus, enough groundwater and sand prone to liquefaction are essential to these landslides that occurred in the Saskatchewa river region. Crosta *et al.* (2015) presented multiple examples of landslides from steep slopes falling onto a shallow erodible substrate or water layer, and then travel long-runout distance with typical high velocity. Crosta and his colleagues have confirmed that the loading processes of the overlying landslide mass resulted in the substrate liquefaction is key to the mobility on a flat area (Crosta *et al.*, 2009a; Crosta *et al.*, 2009b; Crosta *et al.*, 2015; Crosta *et al.*, 2016). The very recent 2014 Oso landslide gained a lot of attentions about its long runout mobility mechanism. The Oso landslide failed on steep slopes, and then move along a nearly flat terrace (Iverson *et al.*, 2015; Iverson and George, 2016; Wartman *et al.*, 2016; Stark *et al.*, 2017; Collins and Reid, 2020). However, these authors argue about the sequential stages of the Oso landslide and what material was liquefied to explain its long runout mobility on the nearly flat alluvial plain.

The aforementioned typical examples improve our understanding of the transformed landslide from slides on steep upper slopes to flow along gently terrace and provide important insight of the base liquefaction of terrace deposits controlling rapid and long-runout mobility, although disagreement remains regarding mechanisms involved. However, these example landslides confirm that the unusual structural and hydrologic configurations on the slope toe and fronted terrace zones are critical for producing a rapid, long-runout landslide overriding terrace deposits.

4.2 Rapid and long-runout mobility overridden on a liquefied substrate

There should be similar transformed and mobilized mechanisms between Saleshan landslide and these landslides mentioned above. The landslides detected on steep upper slopes transformed into flow-type landslides, causing a rapid and long-runout mobility overridden on the sand substrate on the nearly flat or gentle terrace with enough water. Overall, there can divide into two stages after slope failure. One is the instantaneous transformation of movement style at the toe of the slope; the second is then long-runout mobility on the fronted terrace. They are both attributed to dynamic loading from upper landslide mass on the lower liquefied substrate, which is generally composed of alluvial sand and silt of terrace deposits. And consequentially, the impact loading results in the generation of excess pore water pressure on the liquefied sand at the toe of the terrace deposits under undrained condition, causing a dramatic decrease in shear resistance of the saturated sand. Nevertheless, there has an essential difference during transformation and mobility. The transformed moment should be in an undrained condition with almost constant pore water pressure, along with a lower shear resistance. While the mobilized progress is more like a drained condition with almost constant shear resistance, comparing continuously dissipated pore water pressure. Our triaxial dynamic impact loading provides a reasonable explanation for the hypothesized mechanism to transformation and mobility (Figs. 12). This mechanism is consistent with those obtained in physical and numerical simulations performed by other authors (Take and Beddoe, 2014; Crosta et al., 2016; Collins and Reid, 2020).

It is worth to mention another type of the transformed landslide from slide to flow coupled with a channel bed erosion along its flow paths. In these events, the displaced materials after failure entrain and liquefy saturated soil from its flow paths along the channel on a slope (Evans *et al.*, 2001; Wang *et al.*, 2003; Hungr and Evans, 2004; Iverson *et al.*, 2011). There also had a typical case study in Chinee loess areas, i.e., the Dagou loess flowslide with significant entrainment (Peng *et al.*, 2015; Zhang *et al.*, 2017). The underlying process of entrainment and liquefaction is a rapid undrained loading from the overriding landslide mass. As the dynamic undrained loading leads to an increase in pore water pressure (Hutchinson and Bhandari, 1971; Sassa and Wang, 2005; Wang *et al.*, 2013), and liquefy the underlying deposits on the channel (Wang *et al.*, 2013; Collins and Reid, 2020), causing entrainment of landslide with higher volume and greater mobility (Hungr and Evans, 2004). As the channelizing topography can focus landslide momentum (Iverson *et al.*, 2015), and wet bed deposit can enhance its mobilized capacity (Iverson *et al.*, 2011; Iverson *et al.*, 2015). In the study to the 2014 Oso landslide, however, Iverson *et al.* (2015) pointed out that the transformed landslide into a nearly flat surface is unlike virtually all the flow along the channelling path. This is because, as suggested by Hutchinson and Bhandari (1971), the rapid mobility overridden on a nearly flat slope partakes more of mass transport than the mass movement.

Hence, the transformation from slide to flow includes two modes due to topographic differences. However, there is the same increase in pore water pressure in the liquefied substrate triggered by dynamic loading (Fig. 14). Meanwhile, the transformation of the two movement types is both transients to the generation of pore water pressure in the erosional layer, and the followed long-runout mobility depends on topographic change and dissipated time of the pore water pressure.

5. Conclusions

The flowslide overridden on a liquified substrate generally mobilized on a nearly flat flow path, causing rapid long-runout distance and catastrophic threats. We studied the Saleshan landslide of Gansu in China, which is a typical loess flowslide mobilized on the nearly flat terrace with an easily liquefied alluvial sand substrate. The geomorphologic imprints and topographic changes present the different dynamic features and mobilized behaviors at different zones of the Saleshan landslide. And its accumulated features and the placemarks show that the landslide exists a motion transformation from the slide on the steep slope to flow on the gentle terrace with rapid velocity and long-runout distance. Meanwhile, ERT surveying confirms the existence of abundant groundwater in the accumulation zone of the Saleshan landslide, which is crucial to the motion transformation.

Our triaxial shear tests suggest that loess, alluvial sand, and red soil are sensitive to liquefaction at the undrained conditions. Among them, the loess is the easiest liquefaction. The impact loading test results show that the alluvial sand is natural liquefaction at undrained condition while it is difficult to drained condition due to rapid water pore pressure dissipation. This aggravated the occurrence of the mobilized loess. As a result, the progress enhanced the mobilization of the Saleshan landslide on the nearly flat terrace. Overall, we conclude that the hydrologic condition of the terrace is essential to the movement of the Saleshan landslide, and the liquefaction features of the materials are the key to its transformation during the landslide's movement. Meanwhile, this kind of flowslide overridden on the liquified substrate partakes more of mass transport than a mass movement.

Acknowledgments

This study was partially supported by the National Natural Science Foundation of China (Nos. 41977212, 41790443 and 41927806), the National Key Research and Development Program of China (No. 2018YFC504702). Mr. Xishan Lin, Mr. Shuaijun Hu, and Mr. Xiaoming Feng of Lanzhou University are thanked for their help in the field investigation. Yao Jiang acknowledges support from the CAS Pioneer Hundred Talents Program. Images of the geographic, topographic, geomorphic maps and photographs used for this paper are properly cited and referenced. Original data from ERT, particle size distribution and triaxial shear test are available upon request (zhangfy@lzu.edu.cn).

References

Aaron, J., Hungr, O., Stark, T.D., Baghdady, A.K., 2017. Oso, Washington, landslide of March 22, 2014: Dynamic analysis. Journal of Geotechnical & Geoenvironmental Engineering 143.

Bogiatzis, P., 2015. Revitalizing decades-old analog seismograms through image analysis and digitization. Mathwork, Technical Articles and Newsletters, https://www.mathworks.com/company/newsletters/articles/revitalizing-decades-old-analog-seismograms-through-image-analysis-and-digitization.html?s_tid=srchtitle.

Burda, J., Veselý, M., Řehoř, M., Vilímek, V., 2018. Reconstruction of a large runout landslide in the Krušné hory Mts. (Czech Republic). Landslides 15, 423–437.

Carraro, J.A.H., Prezzi, M., Salgado, R., 2009. Shear strength and stiffness of sands containing plastic or nonplastic fines. Journal of Geotechnical and Geoenvironmental Engineering 135, 1167-1178.

Chambers, J., Meldrum, P., Gunn, D., Wilkinson, P., Merritt, A., Murphy, W., West, J., Kuras, O., Haslam, E., Hobbs, P., 2013. Geophysical-geotechnical sensor networks for landslide monitoring. Landslide Science and Practice. Springer, pp. 289-294.

Collins, B.D., Reid, M.E., 2020. Enhanced landslide mobility by basal liquefaction: The 2014 State Route 530 (Oso), Washington, landslide. GSA Bulletin 132, 451-476.

Crawford, M.M., Bryson, L.S., Woolery, E.W., Wang, Z., 2019. Long-term landslide monitoring using soil-water relationships and electrical data to estimate suction stress. Engineering Geology 251, 146-157.

Crosta, G., Imposimato, S., Roddeman, D., 2009a. Numerical modeling of 2 - D granular step collapse on erodible and nonerodible surface. Journal of Geophysical Research: Earth Surface 114.

Crosta, G.B., Blasio, F.V., Caro, M., Volpi, G., Imposimato, S., Roddeman, D., 2016. Modes of propagation and deposition of granular flows onto an erodible substrate: experimental, analytical, and numerical study. Landslides, 1-22.

Crosta, G.B., Blasio, F.V.D., Locatelli, M., Imposimato, S., Roddeman, D., 2015. Landslides falling onto a shallow erodible substrate or water layer: an experimental and numerical approach. IOP Conference Series: Earth and Environmental Science 26, 012004.

Crosta, G.B., Imposimato, S., Roddeman, D., 2009b. Numerical modelling of entrainment/deposition in rock and debris-avalanches. Engineering Geology 109, 135-145.

Derbyshire, E., Meng, X.M., Dijkstra, T.A., 2000. Landslides in the Thick Loess Terrain of North-West China. Wiley.

Dufresne, A., Geertsema, M., 2020. Rock slide–debris avalanches: flow transformation and hummock formation, examples from British Columbia. Landslides, 1-18.

Evans, S.G., Hungr, O., Clague, J.J., 2001. Dynamics of the 1984 rock avalanche and associated distal debris flow on Mount Cayley, British Columbia, Canada; implications for landslide hazard assessment on dissected volcanoes. Engineering Geology 61, 29-51.

Grandjean, G., Gourry, J.C., Sanchez, O., Bitri, A., Garambois, S., 2011. Structural study of the Ballandaz landslide (French Alps) using geophysical imagery. Journal of Applied Geophysics 75, 531-542.

Huang, R., 2009. Some catastrophic landslides since the twentieth century in the southwest of China. Landslides 6, 69-81.

Hungr, O., Evans, S.G., 2004. Entrainment of debris in rock avalanches: An analysis of a long run-out mechanism. Geological Society of America Bulletin 116, 1240-1252.

Hungr, O., Leroueil, S., Picarelli, L., 2014. The Varnes classification of landslide types, an update. Landslides 11, 167-194.

Hutchinson, J.N., Bhandari, R.K., 1971. Undrained loading, a fundamental mechanism of mudflows and other mass movements. Géotechnique 21, 353-358.

Ishihara, K., Okusa, S., Oyagi, N., Ischuk, A., 1990. Liquefaction-induced flowslide in the collapsible loess deposit in Soviet Tajik. Soils and Foundations 30, 73-89.

Iverson, R.M., George, D.L., 2016. Modelling landslide liquefaction, mobility bifurcation and the dynamics of the 2014 Oso disaster. Géotechnique 66, 175-187.

Iverson, R.M., George, D.L., Allstadt, K., Reid, M.E., Collins, B.D., Vallance, J.W., Schilling, S.P., Godt, J.W., Cannon, C.M., Magirl, C.S., Baum, R.L., Coe, J.A., Schulz, W.H., Bower, J.B., 2015. Landslide mobility and hazards: implications of the 2014 Oso disaster. Earth and Planetary Science Letters 412, 197-208.

Iverson, R.M., Reid, M.E., LaHusen, R.G., 1997. Debris-flow mobilization from landslides. Annual Review of Earth and Planetary Sciences 25, 85-138.

Iverson, R.M., Reid, M.E., Logan, M., LaHusen, R.G., Godt, J.W., Griswold, J.P., 2011. Positive feedback and momentum growth during debris-flow entrainment of wet bed sediment. Nature Geoscience 4, 116-121.

Kang, C., Zhang, F., Pan, F., Peng, J., Wu, W., 2018. Characteristics and dynamic runout analyses of 1983 Saleshan landslide. Engineering Geology 234, 181-195.

Kramer, S.L., 1988. Triggering of liquefaction flow slides in coastal soil deposits. Engineering Geology 26, 17-31.

Li, P., Shen, W., Hou, X., Li, T., 2019. Numerical simulation of the propagation process of a rapid flow-like landslide considering bed entrainment: A case study. Engineering Geology 263, 105287.

Ma, J., Qian, J., 1998. Prediction and evaluation of the influence on environmental hydrogeology in nalesi irrigation district of Baxiehe River Basin. Journal of Lanzhou University 34, 106-111.

Mangeney, A., 2011. Landslide boost from entrainment. Nature Geoscience 4, 77-78.

Miao, T., Liu, Z., Niu, Y., Ma, C., 2001. A sliding block model for the runout prediction of high-speed landslides. Canadian Geotechnical Journal 38, 217-226.

Misfeldt, G.A., Sauer, E.K., Christiansen, E.A., 1991. The Hepburn landslide: an interactive slope-stability and seepage analysis. Canadian Geotechnical Journal 28, 556-573.

Paguican, E.M.R., Wyk de Vries, B., Lagmay, A.M.F., 2014. Hummocks: how they form and how they evolve in rockslide-debris avalanches. Landslides 11, 67-80.

Pavoni, N., 1968. Über die Entstehung der Kiesmassen im Bergsturzgebiet von Bonaduz-Reichenau (Graubünden). Eclogae Geol. Helv 61/2, 494–500.

Peng, D., Xu, Q., Zhang, X., Xing, H., Zhang, S., Kang, K., Qi, X., Ju, Y., Zhao, K., 2019. Hydrological response of loess slopes with reference to widespread landslide events in the Heifangtai terrace, NW China. Journal of Asian Earth Sciences 171, 259-276.

Peng, J., Fan, Z., Wu, D., Zhuang, J., Dai, F., Chen, W., Zhao, C., 2015. Heavy rainfall triggered loess–mudstone landslide and subsequent debris flow in Tianshui, China. Engineering Geology 186, 79-90.

Peng, J., Ma, P., Wang, Q., Zhu, X., Zhang, F., Tong, X., Huang, W., 2018. Interaction between landsliding materials and the underlying erodible bed in a loess flowslide. Engineering Geology 234, 38-49.

Peng, J., Wang, G., Wang, Q., Zhang, F., 2017a. Shear wave velocity imaging of landslide debris deposited on an erodible bed and possible movement mechanism for a loess landslide in Jingyang, Xi'an, China. Landslides 14, 1503-1512.

Peng, J., Zhang, F., Wang, G., 2017b. Rapid loess flow slides in Heifangtai terrace, Gansu, China. Quarterly Journal of Engineering Geology and Hydrogeology 50, 106-110.

Perrone, A., Lapenna, V., Piscitelli, S., 2014. Electrical resistivity tomography technique for landslide investigation: A review. Earth-Science Reviews 135, 65-82.

Picarelli, L., 2010. Discussion on "A rapid loess flowslide triggered by irrigation in China". Landslides 7, 203-205.

Poschinger, A.v., Kippel, T., 2009. Alluvial deposits liquefied by the Flims rock slide. Geomorphology 103, 50-56.

Sassa, K., Wang, G., 2005. Mechanism of landslide-triggered debris flows: Liquefaction phenomena due to the undrained loading of torrent deposits. Debris-flow hazards and related phenomena. Springer, pp. 81-104.

Stark, T.D., Baghdady, A.K., Hungr, O., Aaron, J., 2017. Case Study: Oso, Washington, Landslide of March 22, 2014—Material Properties and Failure Mechanism. Journal of Geotechnical and Geoenvironmental Engineering, 05017001.

Sun, D., Bloemendal, J., Rea, D.K., Vandenberghe, J., Jiang, F., An, Z., Su, R., 2002. Grain-size distribution function of polymodal sediments in hydraulic and aeolian environments, and numerical partitioning of the sedimentary components. Sedimentary Geology 152, 263-277.

Taira, A., Scholle, P.A., 1979. Origin of bimodal sands in some modern environments. Journal of Sedimentary Research 49, 777-786.

Take, W.A., Beddoe, R.A., 2014. Base liquefaction: a mechanism for shear-induced failure of loose granular slopes. Canadian Geotechnical Journal, 496-507.

Wang, G., Huang, R., Chigira, M., Wu, X., Lourenço, S.D.N., 2013. Landslide amplification by liquefaction of runout-path material after the 2008 Wenchuan (M 8·0) Earthquake, China. Earth Surface Processes and Landforms 38, 265-274.

Wang, G., Sassa, K., Fukuoka, H., 2003. Downslope volume enlargement of a debris slide-debris flow in the 1999 Hiroshima, Japan, rainstorm. Engineering Geology 69, 309-330.

Wang, G., Sassa, K., Fukuoka, H., Tada, T., 2007. Experimental study on the shearing behavior of saturated silty soils based on ring-shear tests. Journal of Geotechnical and Geoenvironmental Engineering 133, 319-333.

Wang, G., Zhang, D., Furuya, G., Yang, J., 2014. Pore-pressure generation and fluidization in a loess landslide triggered by the 1920 Haiyuan earthquake, China: A case study. Engineering Geology 174, 36-45.

Wang, S., Zhang, Z., Zhan, Z., Liu, H., 1988. On the characteristics and dynamics of the catastrophic Mount Sale landslide, Gansu. Journal Chengdu College of Geology 15, 58-63.

Wartman, J., Montgomery, D.R., Anderson, S.A., Keaton, J.R., Benoît, J., dela Chapelle, J., Gilbert, R., 2016. The 22 March 2014 Oso landslide, Washington, USA. Geomorphology 253, 275-288.

Wheaton, J.M., Brasington, J., Darby, S.E., Sear, D.A., 2010. Accounting for uncertainty in DEMs from repeat topographic surveys: improved sediment budgets. Earth Surface Processes and Landforms 35, 136-156.

Wheaton, J.M., Fryirs, K.A., Brierley, G., Bangen, S.G., Bouwes, N., O'Brien, G., 2015. Geomorphic mapping and taxonomy of fluvial landforms. Geomorphology 248, 273-295.

Wilkinson, P., Chambers, J., Uhlemann, S., Meldrum, P., Smith, A., Dixon, N., Loke, M.H., 2016. Reconstruction of landslide movements by inversion of 4-D electrical resistivity tomography monitoring data. Geophysical Research Letters 43, 1166-1174.

Wu, W., Wang, N., 2006. Landslide hazards in Gansu. Lanzhou University Press, Gansu, China.

Xu, L., Dai, F., Kwong, A., Tham, L., Tu, X., 2009. Analysis of some special engineering-geological problems of loess landslide. Chinese Journal of Geotechnical Engineering 31, 287-293.

Zhang, F., Kang, C., Chan, D., Zhang, X., Pei, X., Peng, J., 2017. A study of a flowslide with significant entrainment in loess areas in China. Earth Surface Processes and Landforms 42, 2295-2305.

Zhang, F., Wang, G., 2018. Effect of irrigation-induced densification on the post-failure behavior of loess flowslides occurring on the Heifangtai area, Gansu, China. Engineering Geology 236, 111-118.

Zhang, F., Wang, G., Kamai, T., Chen, W., 2014. Effect of pore water chemistry on undrained shear behaviour of saturated loess. Quarterly Journal of Engineering Geology and Hydrogeology 47, 201-210.

Zhang, F., Wang, G., Kamai, T., Chen, W., Zhang, D., Yang, J., 2013. Undrained shear behavior of saturated loess with different concentrations of sodium chlorate solution. Engineering Geology 155, 69-79.

Zhang, F., Yan, B., Feng, X., Lan, H., Kang, C., Lin, X., Zhu, X., Ma, W., 2019. A rapid loess mudflow triggered by the check dam failure in a bulldoze mountain area, Lanzhou, China. Landslides 16, 1981-1992.

Zhang, Z., Chen, S., Tao, L., 2002. 1983 Sale Mountain landslide, Gansu Province, China. Reviews in Engineering Geology 15, 149-164.

Zhang, Z., Wang, S., 1984. On the prediction of the occurrence time and the velocity of a potential landslide. Proceedings, 4th International Symposium on Landslides, Toronto, Canada, pp. 145-146.

Zhuang, J., Peng, J., 2014. A coupled slope cutting—a prolonged rainfall-induced loess landslide: a 17 October 2011 case study. Bulletin of Engineering Geology and the Environment 73, 997-1011.

Figure captions

Fig. 1 Geographical location and reviews of the Saleshan landslide. (a) Location of the Saleshan landslide in Gansu Province, China; (b) Landslide inventory of Baxie River catchment; (c) Panoramic photograph of the Saleshan landslide in 1983 (Courtesy of Y. Wang); (d) Panoramic photograph of the Saleshan landslide in 2015.

Fig. 2 Simplified stratigraphic and topographic section of the Saleshan landslide. (a) Before slope failure; (b) After slope failure.

Fig. 3 Geomorphologic map of Saleshan landslide. 1 Depletion zone; 2 Accumulation zone 3 Depressions; 4 Hillocks; 5 Grooves; 6 Hummocks; 7 Main scarp; 8 Minor scarp; 9 Crown cracks; 10 Lateral cracks; 11 Transverse cracks; 12 Radial cracks; 13 Flanks; 14 Contour lines; 15 Gullies; 16 Springs; 17 Baxie River; 18 Jieer reservoir. The boxes indicate photo locations in Fig. 4, respectively.

Fig. 4 Photographs illustrating typical geomorphological imprints of Saleshan landslide in 1983. (a) Sub-vertical main scarp; (b) Head scarp with depression and hillock; (c) Standing cow in accumulation zone; (d) Life-saving tree at the toe (photo from Zhang *et al.*, 2002); (e) Lateral cracks on the east-side at left flank; (f) Transverse cracks on the west-side at right flank; (g) Transverse cracks on the east-side at left flank; (h) Radial cracks at the toe; (i) Loess liquefaction at right flank on accumulation zone; (j) landslide deposition and dammed lake in Baxie River; (k) Buried Jiuer reservoir and transverse cracks; (l) incompletely liquefied loess on the east-side accumulation zone. See Fig. 3 for photo locations.

Fig. 5 Topographic change detection of pre- and post landslide of the Saleshan landslide. (a) The elevation difference map; (b) the areal change distribution; and (c) the volumetric elevation change distribution. Black lines indicate the profile locations in Fig. 6, and red lines show the profile locations of the ERT surveying in Fig. 8.

Fig. 6 The topographic changes of alternative profiles of the Saleshan landslide, and the specified locations see Fig. 5.

Fig. 7 Motion displacement vector at different placemark locations on the Saleshan landslide. 1 Depletion zone; 2 West accumulation zone; 3 Central accumulation zone; 4 East accumulation zone; 5 House location before failure; 6 House location after failure; 7 Ground marks before failure; 8 Ground marks after failure; 9 Tree location before and after failure; 10 Life-saving tree before and after failure; 11 Placemark number.

Fig. 8 Interpreted Wenner ERT sections of four profiles on the Saleshan landslide. Note: the dashed lines are derived from the real topographic profile, and the detailed locations see Fig. 5 and Fig. 6.

Fig. 9 The exemplified particle size distribution of the three types of soils on the Saleshan landslide. (a) Cumulative distribution curves of particle size; (b) Frequent distribution curves of particle size.

Fig. 10 Undrained triaxial test results of the three different specimens at same confining pressures. (a) Deviator stress versus axial strain; (b) Pore water pressure versus axial strain; (c) Effective stress path

Fig. 11 Undrained triaxial test results of the alluvial sand specimens at different confining pressures. (a) Deviator stress versus axial strain; (b) Pore water pressure versus axial strain; (c) Effective stress path

Fig. 12 Triaxial test results from quasi-dynamic impact stress loading of the alluvial sand specimens. (a) drained impact loading condition; (b) undrained impact loading condition.

Fig. 13 Hypothesised sequence from progressive deformation to the catastrophic mobility of the Saleshan landslide.

Fig. 14 Schematic illustration of two types of entrainment. (a) Mobility overridden on the liquefied substrate on nearly flat flow path; (b) Mobility eroded the liquefied layer in relatively steep channel flow path.

Fig. 1

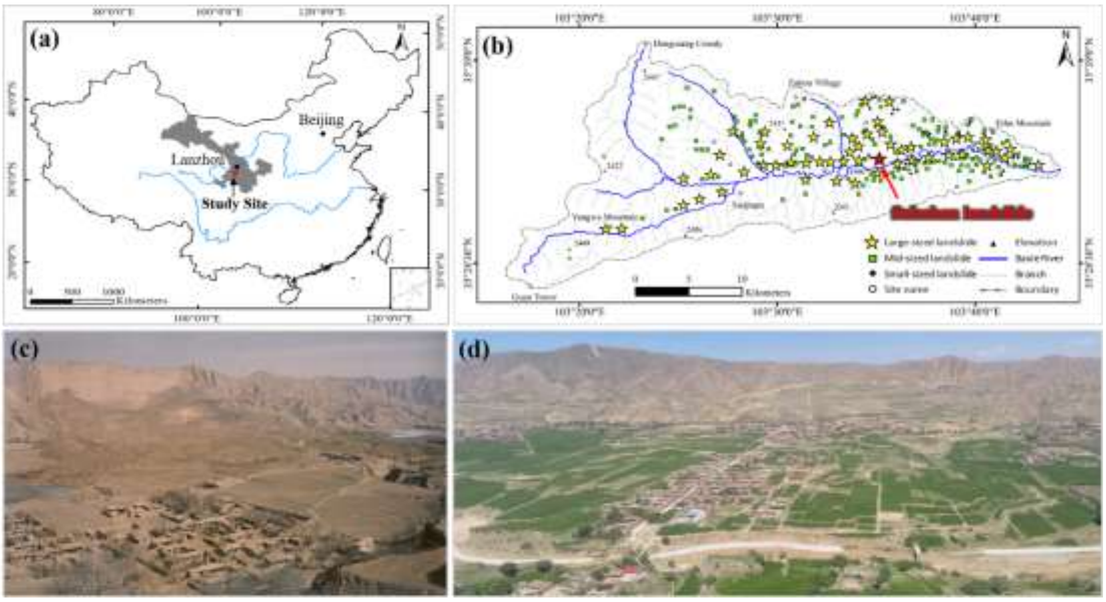

Fig. 2

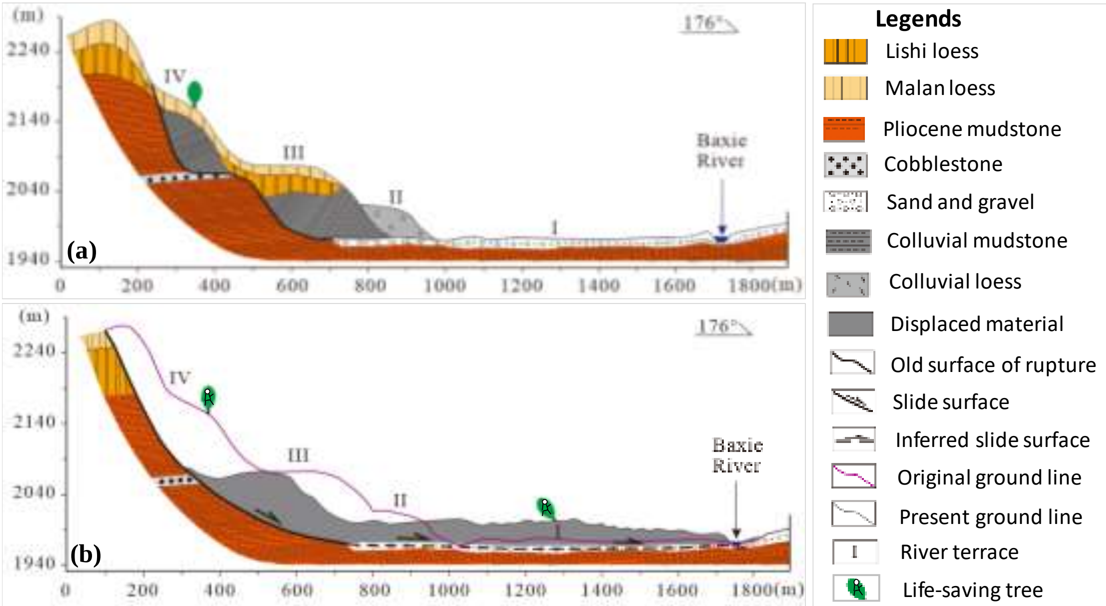
(m)
2240
2140
2040
1940
(a)
0
200
400
600
800
1000
1200
1400
1600
1800(m)
176°
IV
III
II
I
Baxie River
(b)
Legends
Lishi loess
Malan loess
Pliocene mudstone
Cobblestone
Sand and gravel
Colluvial mudstone
Colluvial loess
Displaced material
Old surface of rupture
Slide surface
Inferred slide surface
Original ground line
Present ground line
River terrace
Life-saving tree

Fig. 3

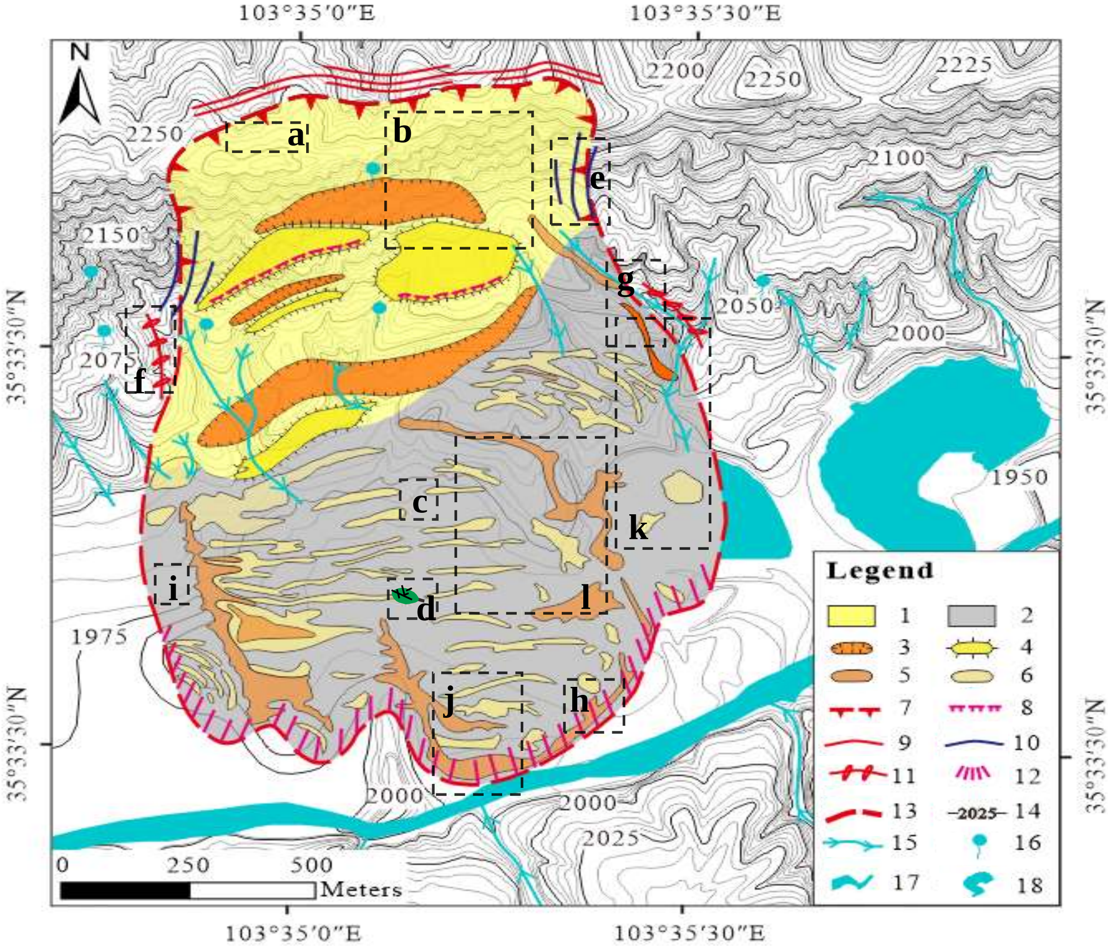
103°35′0″E
103°35′30″E
35°33′30″N
N
2250
2200
2250
2225
2150
2100
2050
2000
1950
207
1975
2000
2000
2025
a
b
c
d
e
f
g
h
i
j
k
l
0
250
500
Meters
Legend
1
2
3
4
5
6
7
8
9
10
11
12
13
2025
14
15
16
17
18

Fig. 4

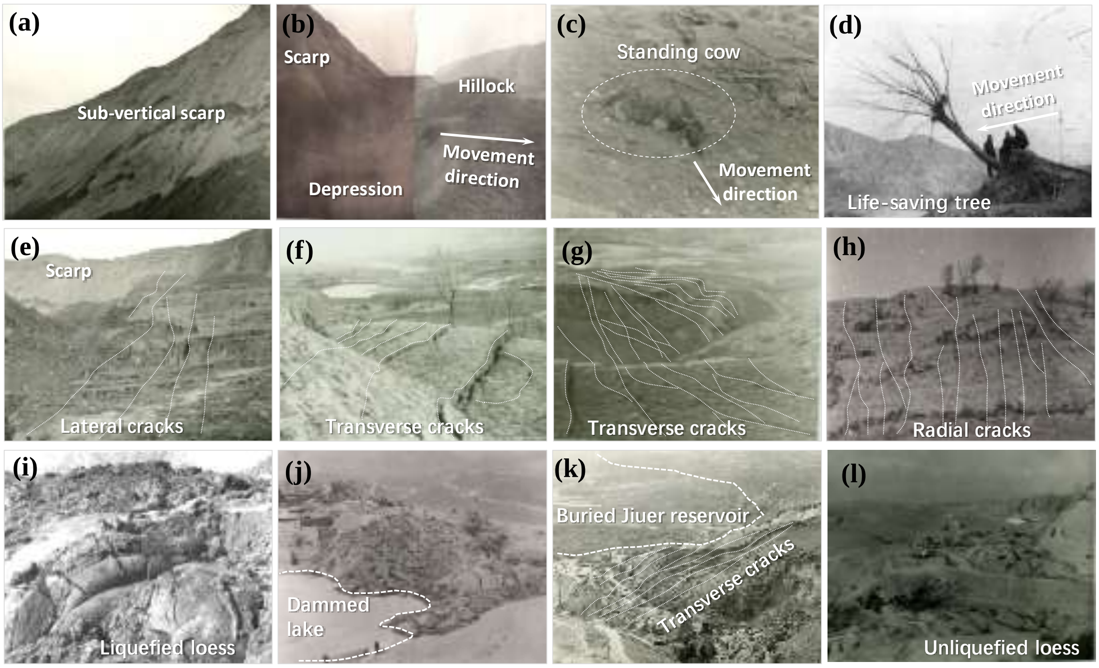
(a)
Sub-vertical scarp
(b)
Scarp
Hillock
Depression
Movement direction
(c)
Standing cow
Movement direction
(d)
Movement direction
Life-saving tree
(e)
Scarp
Lateral cracks
(f)
Transverse cracks
(g)
Transverse cracks
(h)
Radial cracks
(i)
Liquefied loess
(j)
Dammed lake
(k)
Buried Jiuer reservoir
Transverse cracks
(l)
Unliquefied loess

Fig. 5

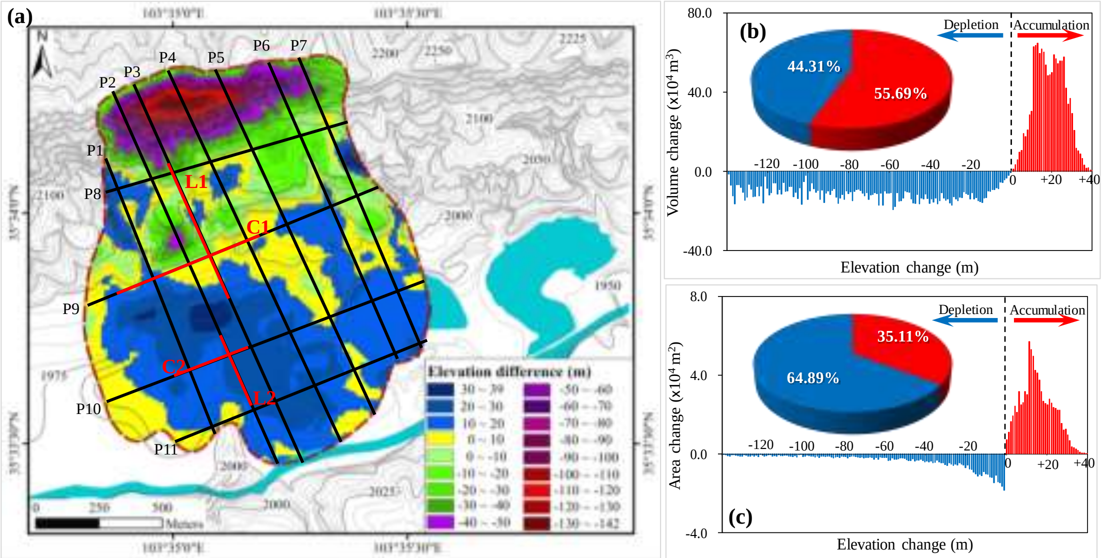
(a)
103°35'0"E
103°35'30"E
35°34'0"N
35°33'30"N
N
P1
P2
P3
P4
P5
P6
P7
P8
P9
P10
P11
L1
L2
C1
C2
Elevation difference (m)
30 ~ 39
20 ~ 30
10 ~ 20
0 ~ 10
0 ~ -10
-10 ~ -20
-20 ~ -30
-30 ~ -40
-40 ~ -50
-50 ~ -60
-60 ~ -70
-70 ~ -80
-80 ~ -90
-90 ~ -100
-100 ~ -110
-110 ~ -120
-120 ~ -130
-130 ~ -142
0 250 500 Meters
(b)
Depletion
Accumulation
44.31%
55.69%
Volume change (x10⁴ m³)
80.0
40.0
0.0
-40.0
-120 -100 -80 -60 -40 -20 0 +20 +40
Elevation change (m)
(c)
Depletion
Accumulation
35.11%
64.89%
Area change (x10⁴ m²)
8.0
4.0
0.0
-4.0
-120 -100 -80 -60 -40 -20 0 +20 +40
Elevation change (m)

Fig. 6

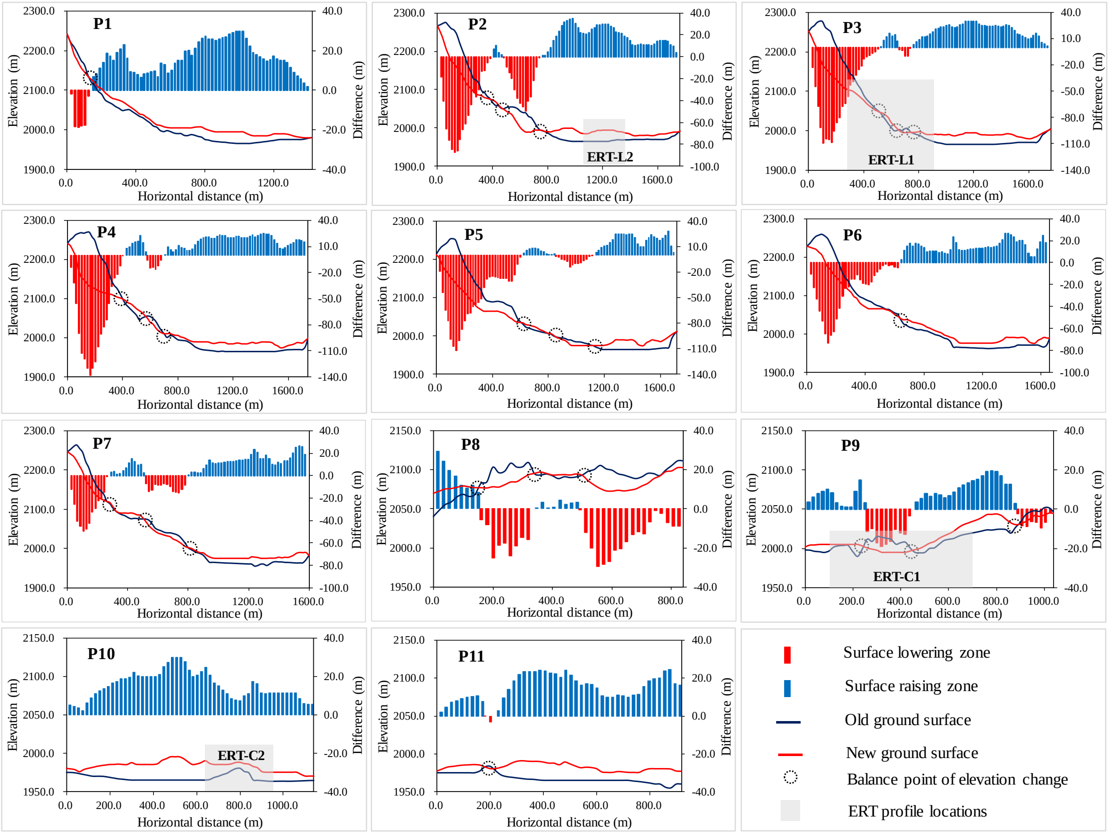
P1
P2
P3
P4
P5
P6
P7
P8
P9
P10
P11
ERT-L2
ERT-L1
ERT-C1
ERT-C2
Elevation (m)
Difference (m)
Horizontal distance (m)
Surface lowering zone
Surface raising zone
Old ground surface
New ground surface
Balance point of elevation change
ERT profile locations

Fig. 7

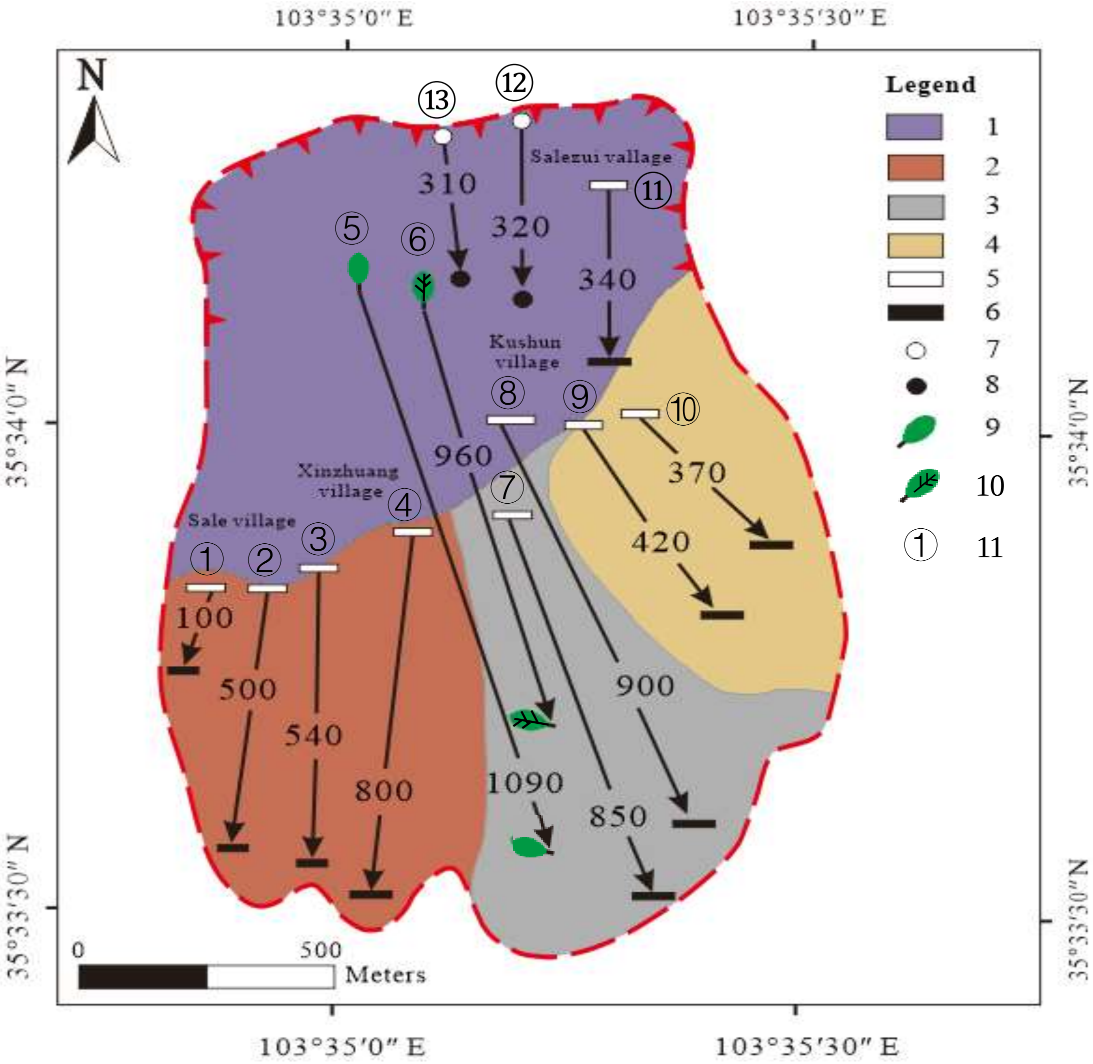
103°35′0″ E
103°35′30″ E
35°34′0″ N
35°33′30″ N
N
Legend
1
2
3
4
5
6
7
8
9
10
11
Salezui vallage
Kushun village
Xinzhuang village
Sale village
⑬
⑫
⑪
⑩
⑨
⑧
⑦
⑥
⑤
④
③
②
①
310
320
340
370
420
960
900
850
1090
800
540
500
100
0
500
Meters

Fig. 8

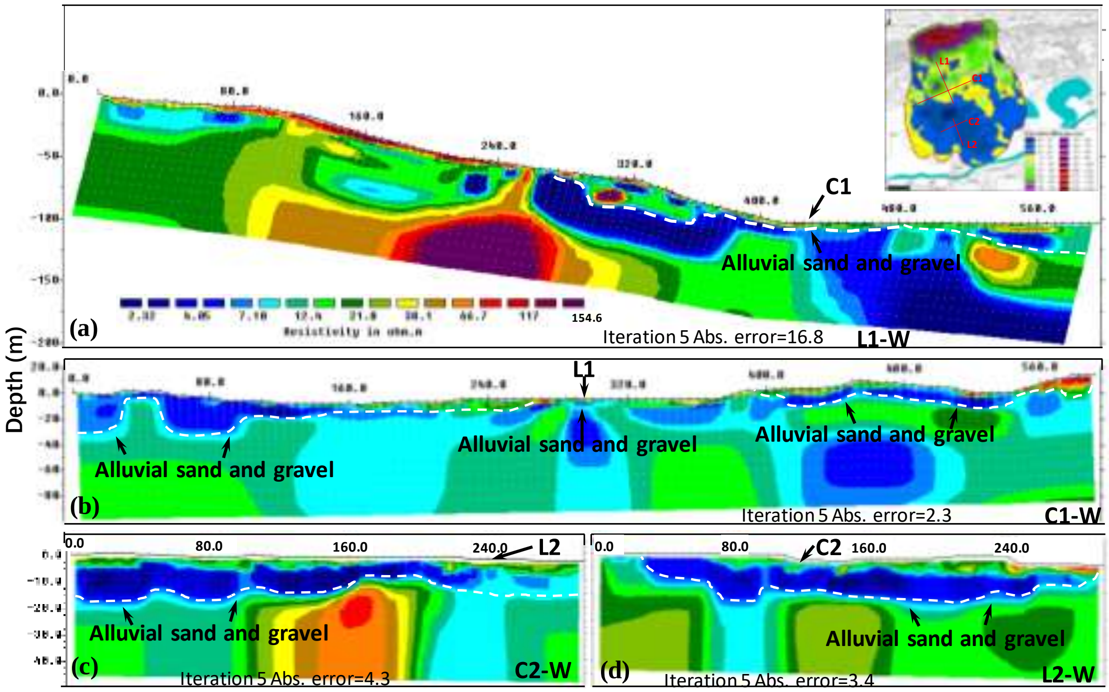

C1
Alluvial sand and gravel
(a)
Iteration 5 Abs. error=16.8
L1-W
154.6
Depth (m)
L1
Alluvial sand and gravel
Alluvial sand and gravel
Alluvial sand and gravel
(b)
Iteration 5 Abs. error=2.3
C1-W
0.0
80.0
160.0
240.0
L2
Alluvial sand and gravel
(c)
Iteration 5 Abs. error=4.3
C2-W
0.0
80.0
C2
160.0
240.0
Alluvial sand and gravel
(d)
Iteration 5 Abs. error=3.4
L2-W

Fig. 9

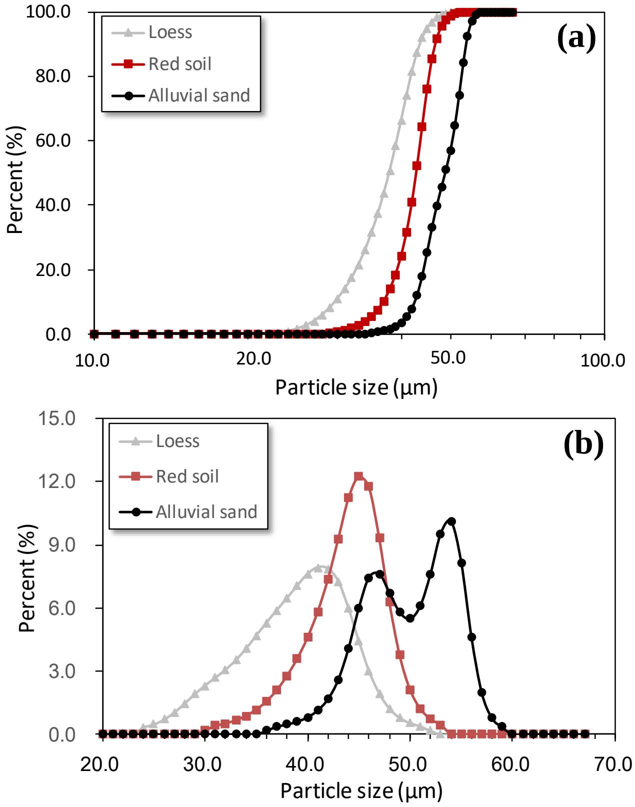
(a)
Loess
Red soil
Alluvial sand
Percent (%)
100.0
80.0
60.0
40.0
20.0
0.0
10.0
20.0
50.0
100.0
Particle size (μm)
(b)
Loess
Red soil
Alluvial sand
Percent (%)
15.0
12.0
9.0
6.0
3.0
0.0
20.0
30.0
40.0
50.0
60.0
70.0
Particle size (μm)

Fig. 10

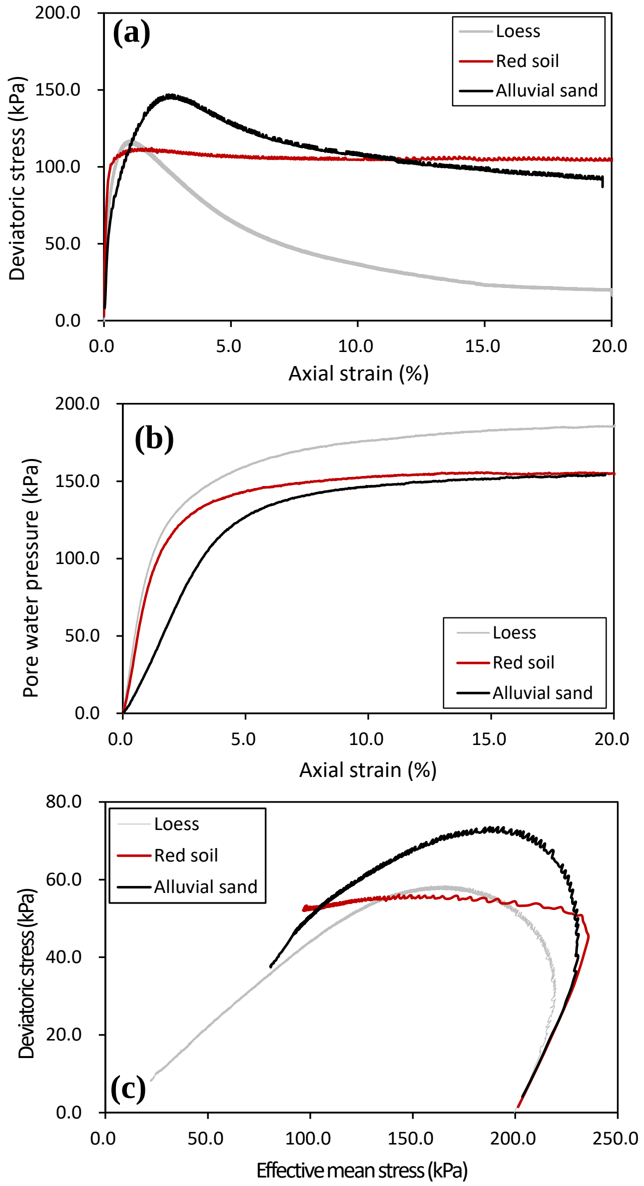
(a)
Loess
Red soil
Alluvial sand
Deviatoric stress (kPa)
Axial strain (%)
(b)
Loess
Red soil
Alluvial sand
Pore water pressure (kPa)
Axial strain (%)
(c)
Loess
Red soil
Alluvial sand
Deviatoric stress (kPa)
Effective mean stress (kPa)

Fig. 11

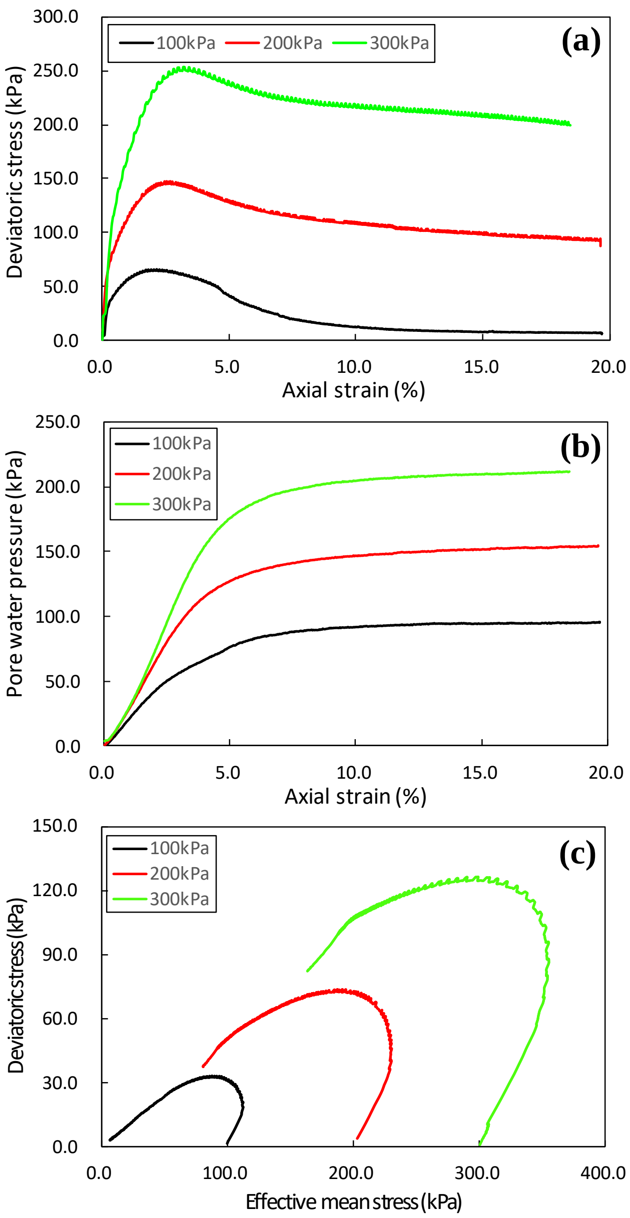

(a)
100kPa
200kPa
300kPa
Deviatoric stress (kPa)
300.0
250.0
200.0
150.0
100.0
50.0
0.0
0.0
5.0
10.0
15.0
20.0
Axial strain (%)
(b)
100kPa
200kPa
300kPa
Pore water pressure (kPa)
250.0
200.0
150.0
100.0
50.0
0.0
0.0
5.0
10.0
15.0
20.0
Axial strain (%)
(c)
100kPa
200kPa
300kPa
Deviatoric stress (kPa)
150.0
120.0
90.0
60.0
30.0
0.0
0.0
100.0
200.0
300.0
400.0
Effective mean stress (kPa)

Fig. 12

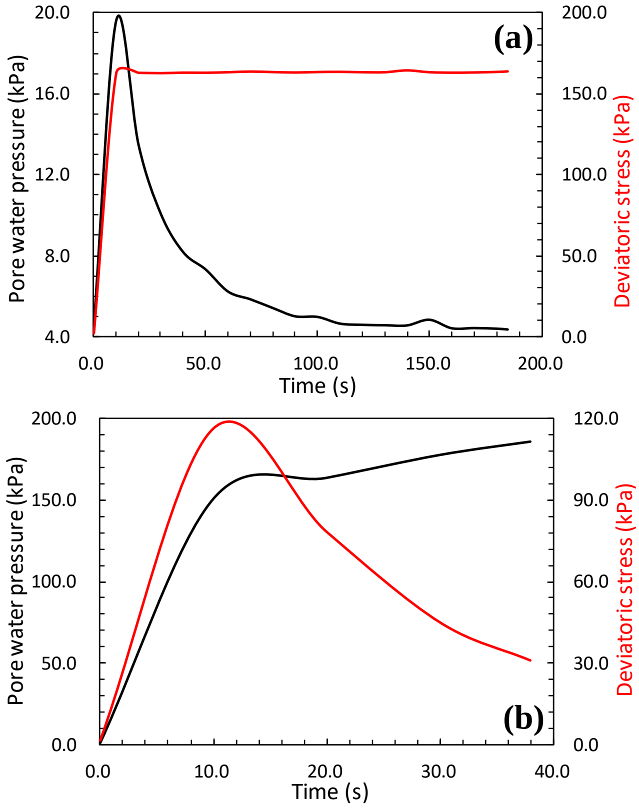
(a)
Pore water pressure (kPa)
20.0
16.0
12.0
8.0
4.0
Deviatoric stress (kPa)
200.0
150.0
100.0
50.0
0.0
Time (s)
0.0
50.0
100.0
150.0
200.0
(b)
Pore water pressure (kPa)
200.0
150.0
100.0
50.0
0.0
Deviatoric stress (kPa)
120.0
90.0
60.0
30.0
0.0
Time (s)
0.0
10.0
20.0
30.0
40.0

Fig. 13

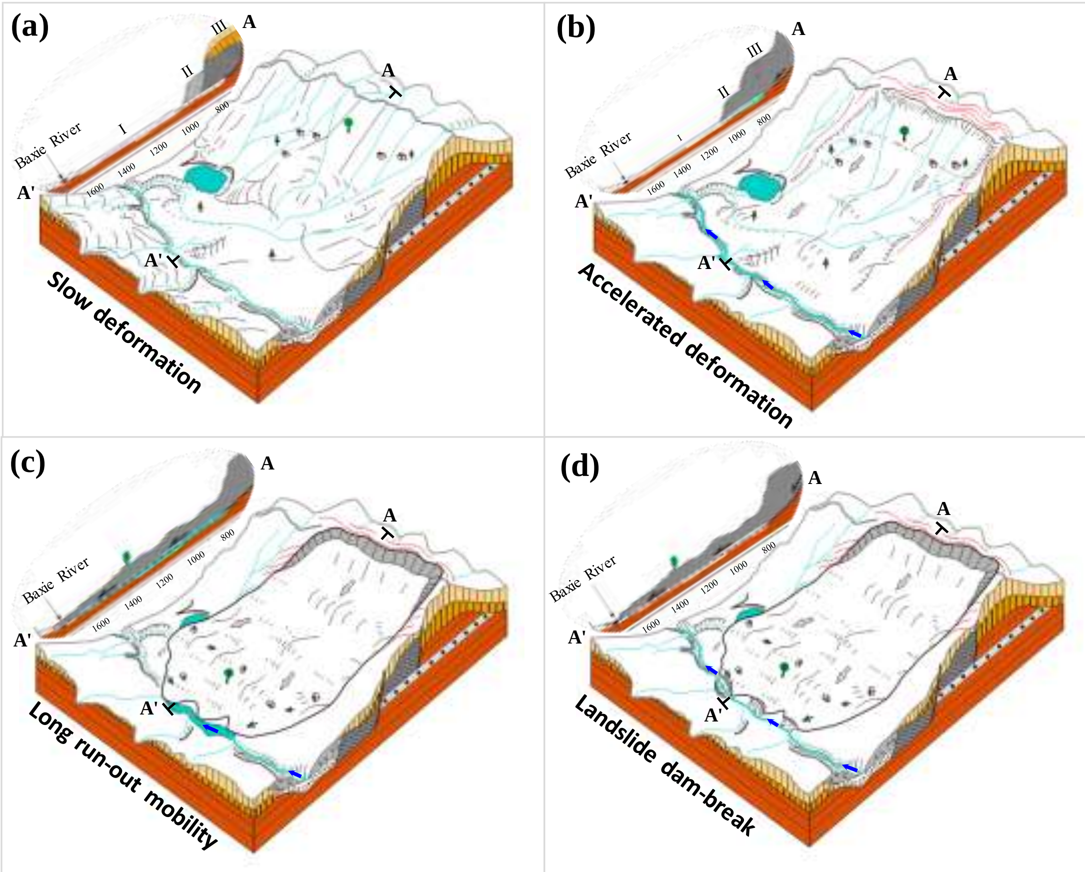
(a)
A
A'
III
II
I
Baxie River
1600
1400
1200
1000
800
Slow deformation
(b)
Accelerated deformation
(c)
Long run-out mobility
(d)
Landslide dam-break

Fig. 14

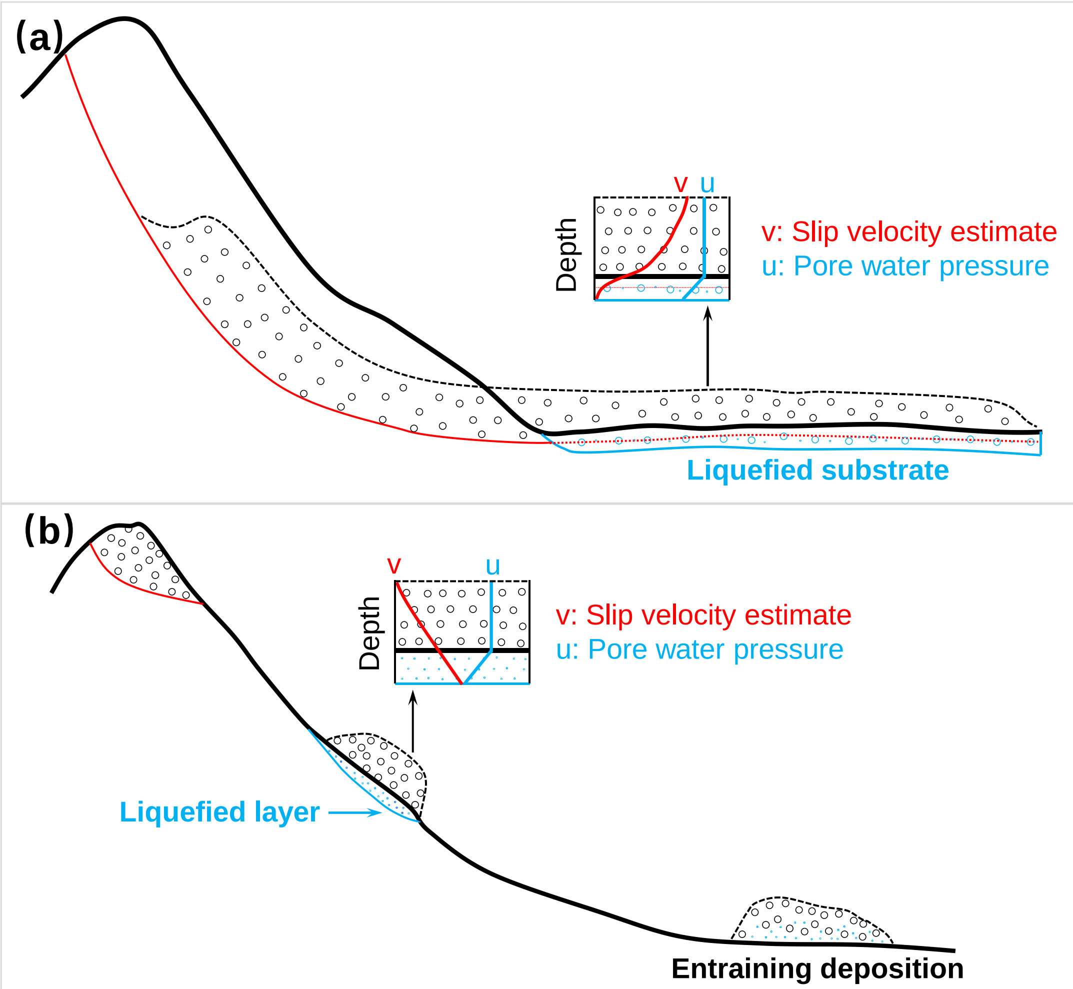
(a)
v u
Depth
v: Slip velocity estimate
u: Pore water pressure
Liquefied substrate
(b)
v u
Depth
v: Slip velocity estimate
u: Pore water pressure
Liquefied layer
Entraining deposition

Table 1: Kinematic parameters of different placemark locations on the Saleshan landslide

No.	PL	TD (°)	HD (m)	V (m/s)	AV (m/s)
1		195	100	1.8	
2	WAZ	187	500	9.1	8.8
3		183	540	9.8	
4		188	800	14.5	
5		167	1090	19.8	
6	CAZ	173	960	17.5	16.7
7		170	850	15.5	
8		166	900	16.4	
9	EAZ	150	420	7.6	7.2
10		149	370	6.7	
11		179	340	6.2	
12	DZ	180	320	5.8	5.9
13		175	310	5.6	

Note, No.: Placemark number; PL: Placemark location; TD: Travel direction; HD: Horizontal displacement; V: Velocity; AV: Average velocity; WAZ: West accumulation zone; CAZ: Central accumulation zone; EAZ: East accumulation zone; DZ: Depletion zone.